

1 **Strength and Stress Evolution of an Actively Exhuming Low-Angle Normal**
2 **Fault, Woodlark Rift, SE Papua New Guinea**

3 **Marcel Mizera¹, Tim Little¹, Carolyn Boulton¹, Yaron Katzir², Nivedita Thiagarajan³,**
4 **David J. Prior⁴, James Biemiller⁵, Euan G.C. Smith¹**

5 ¹School of Geography, Environment and Earth Sciences, Victoria University of Wellington,
6 Wellington, New Zealand.

7 ²Department of Geological and Environmental Sciences, Ben Gurion University of the Negev,
8 Israel.

9 ³Division of Geological and Planetary Sciences, California Institute of Technology, Pasadena,
10 CA 91125

11 ⁴Department of Geology, University of Otago, Dunedin, New Zealand.

12 ⁵Institute for Geophysics, Jackson School of Geosciences, University of Texas at Austin, Austin,
13 Texas, USA.

14 Corresponding author: Marcel Mizera (marcel.mizera@vuw.ac.nz)

15 **Key Points:**

- 16 • The active Mai'iu low-angle normal fault dips $\sim 20^\circ$ at the surface, but is steeper at depth.
- 17 • A differential stress peak of 140–185 MPa at 6–12 km depth was identified in a zone of
18 mixed-mode seismic- and aseismic slip.
- 19 • High differential stresses drive slip on a $\sim 35^\circ$ dipping part of this fault and cause new
20 brittle yielding of strong mafic footwall rocks.
- 21 • The Mai'iu fault is frictionally weak near the surface ($\mu \approx 0.15\text{--}0.38$), but strong in the
22 middle crust ($\mu > 0.25\text{--}0.62$).
- 23 • Reconstructed principal stresses are constrictional and consistent with rolling-hinge style
24 flexure of the footwall.

25 Abstract

26 Quantifying lithospheric strength is essential to better understand seismicity in
27 continental regions. We estimate differential stresses and principal stress orientations driving
28 rapid slip (~10 mm/yr) on the active Mai'iu low-angle normal fault in Papua New Guinea. The
29 fault's mafic footwall hosts a well-preserved sequence of mylonite, foliated cataclasite,
30 ultracataclasite and gouge. In these fault rocks, we combine stress inversion of fault-slip data and
31 paleostress analysis of syntectonically emplaced calcite veins with microstructural and clumped-
32 isotope geothermometry to constrain a syn-exhumational sequence of deformation stresses and
33 temperatures, and to construct a stress profile through the exhumed footwall of the Mai'iu fault.
34 This includes: 1) at ~12–20 km depth ($T \approx 275\text{--}370^\circ\text{C}$), mylonites accommodated slip on the
35 Mai'iu fault at low differential stresses ($>25\text{--}135$ MPa) before being overprinted by localized
36 brittle deformation at shallower depths; 2) at ~6–12 km depth ($T \approx 130\text{--}275^\circ\text{C}$) differential
37 stresses in the foliated cataclasites and ultracataclasites were high enough (>150 MPa) to drive
38 slip on a mid-crustal portion of the fault (dipping $30\text{--}40^\circ$), and to trigger brittle yielding of mafic
39 footwall rocks in a zone of mixed-mode seismic/aseismic slip; and 3) at the shallowest crustal
40 levels ($T < 150^\circ\text{C}$) on the most poorly oriented part of the Mai'iu fault (dipping $\sim 20\text{--}24^\circ$), slip
41 occurred on frictionally weak clay-rich gouges ($\mu \approx 0.15\text{--}0.38$). Subvertical σ_1 and subhorizontal
42 σ_3 parallel to the extension direction, with $\sigma_1 \approx \sigma_2$ (constriction), reflect vertical unloading and 3-D
43 bending stresses during rolling-hinge style flexure of the footwall.

44 **1 Introduction**

45 Lithospheric or crustal strength is often expressed as the maximum differential stress that
46 a rock can sustain before it fractures or flows. Most knowledge of brittle rock strength comes
47 from laboratory experiments (e.g., Byerlee, 1978) and deep boreholes (e.g., Zoback & Harjes,
48 1997; Hickman & Zoback, 2004). These studies typically infer Coulomb frictional failure in the
49 upper crust, in which the differential stress or shear stress (τ) is linearly related to the effective
50 normal stress (σ_e) via a "Byerlee" coefficient of friction ($\mu=0.6\text{--}0.85$, Byerlee, 1978; Behr &
51 Platt, 2014). Detachment faults that may have formed and/or slipped as "low-angle normal
52 faults" ($<30^\circ$, LANFs), remain a controversial topic because Andersonian normal faults in Mohr-
53 Coulomb materials with "Byerlee" frictional strength should initiate and slip at dips of $60\text{--}75^\circ$
54 and frictionally lock-up at dips $<30\text{--}45^\circ$ (e.g., Anderson, 1951; Sibson, 1985; Lister & Davis,
55 1989; Collettini & Sibson, 2001; Axen, 2004, 2007; Collettini, 2011). Yet, a small number of
56 normal faults are demonstrably active today at low angles (dip $<30^\circ$; e.g., Rigo et al., 1996;
57 Chiaraluce et al., 2007, 2014; Hreinsdóttir & Bennett, 2009; Wallace et al., 2014).

58 How crustal strength changes as a function of depth and whether LANFs are weak
59 relative to their surroundings, to other faults, and to laboratory friction values remain
60 fundamental questions in geodynamics (e.g., Axen, 2004; Behr & Platt, 2011 and references
61 therein). Slip on a seemingly misoriented, shallow normal fault in an Andersonian stress regime
62 might be achieved by: (1) high pore fluid pressures within the fault zone (e.g., Axen, 1992;
63 Collettini & Barchi, 2004; Ikari et al., 2009; Abers, 2009); and/or (2) frictionally weak fault
64 materials such as a phyllosilicate-rich (i.e., talc, saponite) gouge (e.g., Floyd et al., 2001;
65 Collettini et al., 2009a, 2009b; Collettini, 2011; Lockner et al., 2011). A third possible
66 mechanism for low-angle slip involves rotation of the principal stress axes to "non-Andersonian"
67 orientations; for example, due to coseismic damage-induced changes in fault zone elastic
68 properties, earthquake rupture dynamics, topographic loads, lateral density variations, and/or
69 horizontal or vertical shear tractions caused by lower crustal flow (e.g., Yin, 1989 and related
70 comments by Buck, 1990; Axen, 2004; Westaway, 2005; Faulkner et al., 2006). Finally, where
71 the near-surface portion of a LANF is convex-up—rather than planar—mechanical resistance to
72 slip may be much reduced (Choi & Buck, 2012; Reston, 2020).

73 Where they bound metamorphic core complexes (MCCs), detachment faults typically
74 record slip magnitudes of tens of kilometres—sufficient to exhume crustal rocks in their footwall

75 from below the brittle-ductile transition (BDT; e.g., Whitney et al., 2013; Platt et al., 2015).
76 Microstructural, paleopiezometric, and geothermometric data from these exhumed rocks can be
77 combined to produce a naturally constrained profile of crustal strength with depth (e.g., Behr &
78 Platt, 2011). Detachment faults are particularly appropriate for such an analysis, because they
79 typically undergo progressive strain localization (e.g., Behr & Platt, 2011; Platt et al., 2015;
80 Cooper et al., 2017) that preserves relicts of older-formed fault rocks in the structurally lower
81 part of the exhumed fault rock sequence (Mizera et al., 2020). Most previously studied examples
82 of MCCs are ancient, and processes that drove slip on these detachments are obscured by
83 combinations of tectonic tilting, erosion, chemical alteration, and other post-slip overprints (e.g.,
84 Axen & Hartley, 1997; Axen, 2004; Collettini, 2011; Whitney et al., 2013); while most known
85 active examples of LANFs are concealed beneath a cover of brittlely faulted upper-plate rocks
86 (e.g., Rigo et al., 1996; Chiaraluce et al., 2014). Exhumed fault rocks are exposed within the ~3
87 km-tall domal footwall of the Mai'iu fault in SE Papua New Guinea, one of the best-preserved
88 active continental LANFs on Earth (e.g., Wallace et al., 2014; Webber et al., 2018). Dip slip on
89 this fault at ~10 mm/yr for the past 3–4 Myrs (Wallace et al., 2014; Webber et al., 2018; Österle
90 et al., 2020) has exhumed a >29 km-wide, little-eroded fault surface in its metabasaltic footwall.
91 Along—and immediately beneath—this fault surface, freshly exhumed microstructures in the
92 host metabasalt are well-preserved (Little et al., 2019; Mizera et al., 2020).

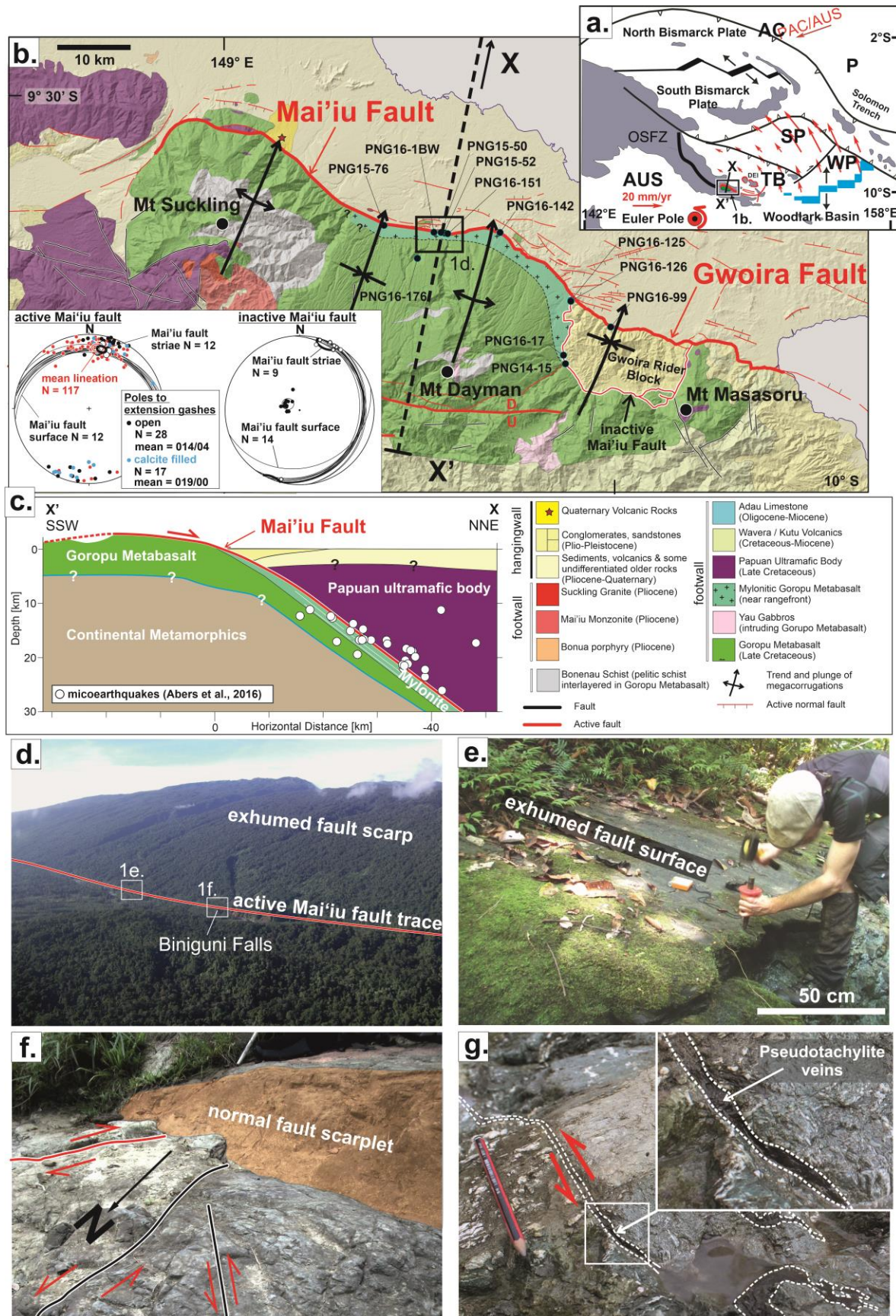
93 In this study, we compile stress-depth snapshots by taking advantage of space-for-time
94 relationships provided by progressive slip localization within the cooling and exhuming footwall
95 of the Mai'iu fault. Estimated differential stresses are based on the mechanical twinning and/or
96 recrystallized grain-size of deformed calcite veins that cross-cut the sequentially formed fault
97 rock units. Deformation temperatures are based on a combination of calcite microstructures (i.e.,
98 calcite-twin morphologies; Ferrill et al., 2004), clumped isotopes in calcite (Stolper & Eiler,
99 2015) and chlorite-composition geothermometry (Cathelineau, 1988; Bourdelle & Cathelineau,
100 2015). We invert for the orientation of principal stresses acting on the fault zone using two
101 datasets: crystallographic data for calcite-twins collected by electron backscatter diffraction, and
102 fault-slip data of late outcrop-scale brittle faults cross-cutting the footwall and hangingwall of the
103 Mai'iu fault. By applying paleostress and geothermometric methods to the sampled fault rock
104 sequence, we reconstruct differential stresses, temperatures and principal stress orientations
105 along the exhumation path of the fault. These datasets are used to infer a stress profile along the

106 Mai'iu fault, from which we derive the fault's peak strength and the integrated strength of the
107 extending brittle crust (see Supporting Information S1 for a detailed explanation of this concept).

108 **2 The Suckling-Dayman Metamorphic Core Complex**

109 The tectonic regime in SE Papua New Guinea is governed by the oblique-convergent
110 motion of the Pacific (PAC) and Australian plates (AUS) at ~100–110 mm/yr (Figure 1a). This
111 collisional motion is absorbed across an intervening mosaic of microplates (Tregoning et al.,
112 1998; Wallace et al., 2004, 2014). Present-day counterclockwise rotation of the Woodlark-
113 Solomon Sea microplate at 2–2.7°/Myr relative to Australia is accompanied by 20–40 mm/yr of
114 seafloor spreading in the oceanic Woodlark Basin and, farther west, by 10–15 mm/yr of
115 extension across the continental Woodlark rift (Wallace et al., 2004). Extension in the Woodlark
116 rift initiated sometime in the interval 3.6–8.4 Ma (Taylor & Huchon, 2002; Little et al., 2007,
117 2011; Fitz & Mann, 2013). Extension near the western end of the Woodlark rift is
118 accommodated primarily by slip on the Mai'iu fault. There, cosmogenic nuclide concentrations
119 from the exposed Mai'iu fault scarp indicate a late Holocene dip-slip rate of 11.7 ± 3.5 mm/yr
120 (Webber et al., 2018), and geodetic data confirm a present-day dip-slip rate of 7.5–10.2 mm/yr
121 (Wallace et al., 2014; Biemiller et al., 2020).

122



124 **Figure 1.** a) Simplified tectonic map of the Woodlark Rift (after Wallace et al., 2004). Locations
 125 of Figure 1b and cross-section X-X' of Figure 1c are highlighted. b) Geological and structural
 126 map of the Suckling-Dayman Metamorphic Core Complex (after Smith & Davies, 1976; Lindley
 127 et al., 2014; Little et al., 2019). Sample locations for this study (black dots) are labelled on this
 128 map (e.g., “PNG16-126”). Inset, lower-hemisphere, equal-area stereograms of fault kinematic
 129 data collected in the mylonitic footwall of the Mai'iu fault <300 m up-dip from its trace: left
 130 stereogram, measured attitudes of the Mai'iu fault surface (black great circles), trend and plunge
 131 of wear striae on the Mai'iu fault surface (white dots) and mylonitic lineation (red dots), poles of
 132 extension gashes that are either open (black dots) or filled with calcite (light blue dots); right
 133 stereogram, attitudes of a now inactive part of the Mai'iu fault that has been tilted eastward on
 134 the limb of the synclinally folded Gwoira rider block at location PNG16-17 (black great circles);
 135 trend and plunge of wear striae on the Mai'iu fault at this location (white dots) are also shown. c)
 136 Tectonic cross-section of the Mai'iu fault (after Little et al., 2019). Microearthquake foci (open
 137 white dots) are based on Abers et al. (2016). d) Oblique aerial photograph of the active Mai'iu
 138 fault rangefront scarp covered in rainforest looking SE. For location see box in part b). e)
 139 Youngest, most recently exhumed surface of the active Mai'iu fault at the base of its scarp
 140 (PNG15-50). f) Outcrop photograph (PNG16-1BW) showing the exhumed mylonitic footwall of
 141 the Mai'iu fault cross-cut by a dip-slip normal fault (orange shading) and dextral and sinistral
 142 strike-slip faults. g) Outcrop photograph of the foliated cataclasite exposed in the footwall of the
 143 E-tilted, inactive part of the Mai'iu fault trace (PNG16-17). Inset shows a sinistral strike slip
 144 fault with pseudotachylite on the slip surface. PAC—Pacific plate; AUS—Australian plate;
 145 WP—Woodlark plate; SP—Solomon-Sea plate; TB—Trobriand block; DEI—D'Entrecasteaux
 146 Islands; OSFZ—Owen-Stanley Fault Zone.

147
 148 The Mai'iu fault bounds the Suckling-Dayman Metamorphic Core Complex (SDMCC,
 149 Figure 1b). Wear striae preserved on the Mai'iu fault surface trend 009–015° (Figure 1b, inset),
 150 subparallel to the current velocity of the Woodlark-Solomon Sea microplate relative to Australia
 151 as derived from elastic block modelling of campaign GPS data (Wallace et al., 2014), and to the
 152 trend of numerous corrugations in the footwall of the SDMCC (Spencer, 2010; Daczko et al.,
 153 2011; Little et al., 2019; Mizera et al., 2019). On average, the Mai'iu fault dips $\sim 22 \pm 2^\circ$ to the
 154 NNE where it emerges from the Holocene alluvial gravel of its hangingwall, and locally it dips

155 as little as $\sim 16^\circ$ at the surface (Figure 1b, inset). Downdip of the surface trace, and aligned with
156 it, microearthquake foci scattered between 12 and 25 km depth define an actively slipping
157 deformation zone dipping north at $30\text{--}40^\circ$ (Figure 1c; Abers et al., 2016). This deformation zone
158 is interpreted as the subsurface continuation of the Mai'iu fault (Abers et al., 2016; Little et al.,
159 2019). The Mai'iu fault is thought to have extensionally reactivated part of the Owen-Stanley
160 thrust—a Late Cretaceous-Paleocene subduction thrust (Webb et al., 2008; Daczko et al., 2011).
161 The Owen-Stanley thrust formed during the obduction of an oceanic and island arc upper plate
162 (the Late-Cretaceous Papuan Ultramafic Belt; PUB) over an oceanic marginal basin and
163 Australian Plate-allied continental margin rocks (Davies, 1978; Webb et al., 2008; Daczko et al.,
164 2009). The Mai'iu fault footwall consists of MORB-derived metabasaltic rocks of $>3\text{--}4$ km
165 thickness with minor interbedded phyllitic metasediments, limestone and chert, known as the
166 Goropu Metabasalt (Figure 1b; Smith & Davies, 1976).

167 To the east of the SDMCC at location PNG16-17 (Figure 1b, inset), an inferred inactive
168 part of the Mai'iu fault dips $16\pm 3^\circ$ to the ESE and is overlain by a fault slice of the Plio-
169 Pleistocene Gwoira Conglomerate. This slice of former hangingwall comprises a rider block
170 (following Choi & Buck, 2012; Reston, 2020) that formed when part of the Mai'iu fault was
171 abandoned upon inception of a younger and more steeply dipping splay of the Mai'iu fault called
172 the Gwoira fault (Webber et al., 2020). The dips of sedimentary growth strata in the rider block
173 and tilting of a flight of late Quaternary fluvial terraces record progressive synclinal folding and
174 southward back-tilting of the rider block, some of which continues today (Mizera et al., 2019;
175 Webber et al., 2020).

176 **2.1 Mai'iu Fault Rocks**

177 The footwall of the Mai'iu fault exposes a self-exhumed sequence of mostly mafic-
178 composition fault rocks (Figures 1d and 1e; in detailed described in Little et al., 2019, Mizera et
179 al., 2020, and Biemiller et al., 2020). From bottom to top, they include: a) nonmylonitic
180 greenschist (protolith); b) mylonite (derived from the protolith); c) foliated cataclasite; d)
181 ultracataclasite; and e) saponite-rich gouge. The fault rocks contain multiple generations of
182 deformed calcite veins, except for the gouge layer, which contains only broken, reworked
183 fragments of former calcite and dolomite veins (Mizera et al., 2020).

184 The mylonite unit (mylonites) is at least 60 m thick along the northern active range front,
185 thinning southward to as little as 1.5 m farther up-dip of the frontal trace (at location PNG16-17,
186 Fig. 1b). The mylonitic rocks are LS-tectonites with a well-defined NNE-trending stretching
187 lineation and late Neogene, normal-sense shear fabrics. Based on pseudosection modelling of
188 their mineral assemblage (epidote, actinolite, chlorite, albite, titanite, \pm quartz, \pm calcite), the
189 mylonites are inferred to have been exhumed from $\sim 25 \pm 5$ km depth with peak metamorphic
190 temperatures of $425 \pm 50^\circ\text{C}$ and pressures of 5.9–7.2 kbar (Daczko et al., 2009). Well-exposed on
191 the exhumed fault surface immediately south of the fault trace, small-offset (slip < 1.5 m) brittle
192 faults cross-cut the fault surface and mylonites. These faults comprise: a) steep, 50° – 75° down-
193 to-the-north dipping, synthetic normal faults; and b) near-vertical strike-slip faults (Figure 1f;
194 Supporting Information S2). The latter occur as a conjugate set of ENE-striking dextral and NW-
195 striking sinistral faults that mutually cross-cut one another. Steeply-dipping, late-stage extension
196 (to mixed shear-extension) gashes cross-cut the mylonites at a high angle to the foliation and
197 strike nearly orthogonal to both the direction of fault slip and the mean trend of mylonitic
198 lineations (Figure 1b, inset). In the rider block, sedimentary beds of the Gwoira Conglomerate
199 are cross-cut by mostly moderate to steeply dipping normal faults that dip variably to the north
200 and south (Supporting Information S2).

201 The mylonites were overprinted and reworked into a structurally overlying, ~ 3 – 1.5 m
202 thick foliated cataclasite unit (foliated cataclasites). The cm- to mm-spaced foliation in the
203 foliated cataclasites is defined by light-coloured albite and quartz \pm calcite-rich domains and
204 darker phyllosilicate (predominantly chlorite)-rich folia. Meter-to-micro-scale normal and strike-
205 slip faults are more densely developed—but less systematically oriented—in the foliated
206 cataclasites (Supporting Information S2). Figure 1g shows a sinistral strike-slip fault that is
207 coated with an inferred pseudotachylite vein. Multiple generations of such black-colored, ultra-
208 fine-grained veins up to 40 mm-thick cross-cut the foliated cataclasites, in some cases with clear
209 injection features. Five pseudotachylite samples with confirmed glassy matrices were dated by
210 $^{40}\text{Ar}/^{39}\text{Ar}$ geochronology; the ages (interpreted as minimum ages for friction melting) range from
211 2.24 ± 0.29 Ma to 3.00 ± 0.43 Ma (Little et al., 2019).

212 The foliated cataclasites are structurally overlain by a ~ 5 – 40 cm thick ultracataclasite unit
213 (ultracataclasites; Figure 1e). The ultracataclasites contain remnant mafic minerals and older
214 (recycled) ultracataclasite fragments embedded in a clay-rich (predominantly corrensites and/or

215 saponite) matrix. The ultracataclasites are sharply overlain by one or more layers of incohesive
216 saponite-rich gouge up to 12 cm thick. The upwardly-thinning arrangement of progressively
217 lower-temperature-formed fault rock units, each of which reworks the subadjacent rocks, is
218 interpreted as a strain-localizing time sequence (Little et al., 2019; Mizera et al., 2020). In the
219 rider block, a sharp, planar slip surface places the unmetamorphosed Gwoira Conglomerate
220 (former hangingwall) against the saponite-rich gouge. Clasts in the Gwoira Conglomerate are
221 cemented by calcite.

222 **3 Methods**

223 **3.1 Structural Measurements, Thin Section Preparation and Microstructural Analysis**

224 Structural measurements and fault rock samples were collected in the footwall and former
225 hangingwall (Gwoira Conglomerate) of the Mai'iu fault (sample locations in Figure 1b).
226 Samples were cut parallel to lineation (or wear striae) and perpendicular to foliation. An optical
227 microscope was used to identify calcite veins in over 100 thin sections. We selected a
228 representative suite of 15 samples spanning the several fault rock units to be prepared into
229 ultrapolished sections. These samples were polished with diamond paste and SYTON (silica
230 suspension; Fynn & Powell, 1979). Fragile specimens were dried for 24 hours at 50°C and
231 impregnated with epoxy prior to polishing.

232 Calcite microstructures in polished sections were analysed with a SIGMA-VP field
233 emission gun scanning electron microscope (FEG-SEM) equipped with an electron backscatter
234 diffraction (EBSD) detector at the University of Otago, using 30 kV acceleration voltage, 50–
235 100 nA beam current, 20–30 mm working distance and 70° sample tilt. Electron backscatter
236 patterns were collected by an HKL Nordlys camera and processed and indexed with the AZTEC
237 software by Oxford Instruments. To resolve the microstructures of calcite veins, step sizes of
238 0.2–1.5 µm were used.

239 **3.2 Paleostress Analysis**

240 *Calcite twinning paleopiezometry*

241 Mechanical twinning on e-planes $\{01\bar{1}8\}$ (using hexagonal structural cell indices) in
242 calcite, for which the shear displacement is in the direction $\langle 0\bar{2}21 \rangle^+$ (positive sense; Barber &
243 Wenk, 1979; De Bresser & Spiers, 1997), is the result of crystal-plastic deformation at

244 temperatures below 400°C (Groshong, 1988). E-twinning in calcite depends on the orientation of
245 stress and attainment of the critical resolved shear stress (CRSS; 2–12 MPa) along the shear
246 direction on any of the three symmetrically equivalent lattice e-planes (e.g., Jamison & Spang,
247 1976; Tullis, 1980; Burkhard, 1993; Lacombe & Laurent, 1996; Yamaji, 2015). The e-twin
248 density in a calcite grain is dependent on differential stress and independent of grain size (Rowe
249 & Rutter, 1990; Rybacki et al., 2013; Brandstätter et al., 2017). The width of a calcite e-twin is
250 mainly a function of temperature and is only weakly dependent on strain, strain rate or stress
251 (e.g., Rowe & Rutter, 1990; Burkhard, 1993; Ferrill et al., 2004). Twin morphology can provide a
252 rough estimate of deformation temperature (Burkhard, 1993; Ferrill et al., 2004).

253 Crystallographic orientation data for adjoining calcite-twin pairs in calcite veins cross-
254 cutting the Mai'iu fault rocks were collected and mapped using EBSD. For each calcite grain, we
255 measured: a) the width of e-twins; and b) the twin density. The latter was determined by
256 counting the number of e-twin lamellae of a given twin set perpendicular to the twin boundaries
257 of individual grains normalized to a unit length of 1 mm (Rybacki et al., 2011; Supporting
258 Information S3). Differential stresses were estimated using the experimentally calibrated twin-
259 density paleopiezometer of Rybacki et al. (2013):

$$260 \quad \sigma_{Diff} = (19.5 \pm 9.8)\sqrt{N_L}, \quad (\text{Eq. 1})$$

261 where N_L is the number of e-twins per mm. This paleopiezometer employs conditions relevant to
262 medium to lower greenschist-facies rocks (>20 to 350°C) that have been deformed to high
263 strains, and is thus best-suited to the calcite veins in our study. For comparison, results from this
264 and two other twin-density paleopiezometers are shown in Supporting Information S3.

265

266 *Recrystallized grain-size paleopiezometry*

267 Dynamic recrystallization of calcite may occur at deformation temperatures >250°C (e.g.,
268 Evan & Dunne, 1991; Weber et al., 2001). The mean recrystallized grain size of calcite is a
269 function of differential stress and can be measured from EBSD maps (e.g., Valcke et al., 2015).
270 We followed the EBSD-based procedure of Cross et al. (2017) to measure calcite grain sizes in
271 veins cross-cutting the Mai'iu fault rocks, and to identify the subset of grains that are
272 recrystallized (detailed description in Supporting Information S4). Differential stresses were then
273 calculated from the average grain size of recrystallized calcite using the paleopiezometer

274 calibrations by Valcke et al. (2015; $K_{\text{EBSD}}=10^{1.9\pm 0.2}$; $p_{\text{EBSD}}=-0.6\pm 0.1$), and Platt and De Bresser
 275 (2017; $K_{\text{OPT}}=10^{3.1\pm 0.3}$; $p_{\text{OPT}}=-1.09(+0.14; -0.18)$):

$$276 \quad D_X = K_X \cdot \sigma_{\text{Diff}}^{-p_X}, \quad (\text{Eq. 2})$$

277 where D_X is the average grain size, K_X and p_X are constants. Calculated differential stresses with
 278 both paleopiezometers by Valcke et al. (2015) and Platt and De Bresser (2017) are shown in
 279 Supporting Information S4.

280

281 *Principal Stress Orientations*

282 Fault slip data (fault attitude, striation direction, sense of slip) were collected in the field
 283 for 54 brittle faults cutting the $\sim 20\text{--}24^\circ$ -dipping exhumed plane of the active Mai'iu fault within
 284 the mylonites and foliated cataclasites near the base of the fault scarp (<300 m updip of the trace)
 285 at 8 locations, and for 30 brittle faults cutting the sedimentary beds of the Gwoira Conglomerate
 286 at 21 locations across the rider block. Markers indicating sense of offset included the exhumed
 287 surface of the Mai'iu fault (footwall), bedding in the Gwoira Conglomerate (hangingwall), and
 288 steeply dipping quartz or calcite veins (best for strike-slip faults cutting the exhumed footwall).
 289 Slip directions were inferred from wear striae or calcite fibres (fault surface veins). The fault
 290 kinematic data were inverted to determine best-fit orientations of principal stress axes (σ_1 and σ_3)
 291 and the stress ratio (Φ), where

$$292 \quad \Phi = \frac{(\sigma_2 - \sigma_3)}{(\sigma_1 - \sigma_3)}. \quad (\text{Eq. 3})$$

293 By definition, the stress ratio (Φ) is 0 for $\sigma_1 > \sigma_2 = \sigma_3$ (axial compression) and 1 for $\sigma_1 = \sigma_2 > \sigma_3$
 294 (axial constriction).

295 Calcite-twin data (pairs of adjacent twinned and untwinned c-axis crystallographic
 296 orientations from EBSD analysis) were also used to invert for paleostress directions. The
 297 twinning data were recast into a form analogous to fault-slip data using the following steps (e.g.,
 298 Turner, 1962; Groshong, 1975; Engelder, 1979; Kilsdonk & Wiltschko, 1988; Craddock &
 299 Magloughlin, 2005; Jaya & Nishikawa, 2013; Kanai & Takagi, 2016): 1) crystallographic
 300 orientation data from host calcite grains (N=912) and their adjacent e-twins (N=3937) were
 301 collected by EBSD; 2) the crystallographic orientations from the e-twin and the host calcite
 302 grains were used to determine the e-twin plane, glide direction, and sense of shear for every twin
 303 pair based on the known angular relationships (e.g., Burkhard, 1993); and 3) the kinematic data
 304 (glide plane, direction, and shear sense) were converted from a sample coordinate system

305 (relative to lineation, foliation, and top-bottom) to a geographical one (N–S, E–W, and top–
306 bottom; see Data Repository for the conversion MATLAB-code).

307 To analyse both of the above datasets, we use the multiple inverse method (MIM) by
308 Yamaji (2000) to invert the kinematic observations for best-fit stress orientations and values of
309 the stress ratio parameter, Φ (Eq. 3). For the calcite-twin data, we compare the results of the
310 Yamaji (2000) algorithm with those of three other tensor inversion techniques applied to calcite
311 twinning data (P-, B- and T-axes calculations after Turner, 1953; strain-gage technique after
312 Groshong 1972, 1974; dihedral calculation after Angelier & Mechler, 1977; see Tables S5.1 and
313 S5.2 in Supporting Information S5). All of them yielded statistically indistinguishable best-fit
314 stress orientations (Supporting Information Figure S5). An advantage of the MIM is that it self-
315 correlates fault-slip data by dividing a set of faults into subsets that might represent the
316 component stress field acting on that subset of the data. The number of subsets equals the
317 binomial coefficient ${}_N C_k = N! / (k!(N-k)!)$, where N is the total number of fault-slip (or calcite twin)
318 data and k the number of elements comprising a subset. The value k is recommended to be 4 or 5
319 (Yamaji, 2000). The reliability of this method depends on the number of collected data, the
320 spatial or temporal heterogeneity of the stress state and the number of subsets that can be
321 correlated to one another (Yamaji, 2000; Otsubo & Yamaji, 2006; Otsubo et al. 2008).

322 **3.3 Clumped-isotope Geothermometry of Calcite**

323 Carbonate ‘clumped isotopes’ are utilized to reconstruct past formation temperatures in
324 carbonate minerals based on the temperature dependent ordering of ^{13}C and ^{18}O atoms into bonds
325 with each other in the same carbonate molecule (Ghosh et al., 2006; Eiler, 2011). We analyzed
326 18 calcite samples from the Mai’iu fault footwall and two calcite cement samples from the
327 Gwoira Conglomerate for carbon, oxygen and clumped isotopes. Analyses were performed on 7–
328 12 mg of individual aliquots of reference materials and unknown calcite samples at Caltech using
329 previously established procedures (Ghosh et al., 2006; Huntington et al., 2009; Passey et al.,
330 2010; Dennis & Schrag, 2010). Briefly, the carbonate materials were digested in phosphoric acid
331 at 90°C to produce CO_2 . The CO_2 was purified from H_2O , trace organics and other contaminants
332 by using a dry ice/ethanol trap and a gas chromatograph with a Porapak Q 120/80 mesh column
333 held at -20°C. The resulting CO_2 was purified again using dry ice/ethanol and nitrogen traps and
334 introduced into a dual inlet Finnigan MAT-253 mass spectrometer. Masses 44–48 were

335 simultaneously collected to obtain Δ_{47} , Δ_{48} , $\delta^{13}\text{C}$ and $\delta^{18}\text{O}$ values. We define R^{47} as the
 336 abundance of mass 47 isotopologues divided by the mass 44 isotopologue. Δ_{4x} is reported
 337 relative to a stochastic distribution of isotopologues for the same bulk isotopic composition. For
 338 example, Δ_{47} is equal to $((R^{47}_{\text{measured}}/R^{47}_{\text{stochastic}})-1)-((R^{46}_{\text{measured}}/R^{46}_{\text{stochastic}})-1)-$
 339 $((R^{45}_{\text{measured}}/R^{45}_{\text{stochastic}})-1))*1000$. Δ_{48} was monitored to detect any hydrocarbon contamination.
 340 Measurements of each gas were done at 16V of mass 44 and consisted of 8 acquisitions, each of
 341 which involved 7 cycles of sample-standard comparison with an ion integration time of 26s per
 342 cycle. Internal standard errors for Δ_{47} averaged 0.02%.

343 $\delta^{13}\text{C}_{\text{VPDB}}$ and $\delta^{18}\text{O}_{\text{VSMOW}}$ values of samples and standards were calculated from raw ion
 344 currents of mass 44–46 using “Brand” parameters (Brand et al., 2010). The Δ_{47} raw data was
 345 corrected for instrument nonlinearity and scale compression (Passey et al., 2010). Several heated
 346 and equilibrated gases of various bulk isotopic compositions were run during each session. These
 347 gases were then used to convert measurements into the interlaboratory absolute reference frame
 348 (ARF; Dennis & Schrag, 2010). Finally, $\Delta_{47,\text{ARF}}$ was converted to temperature using the
 349 Bonifacie calibration (Bonifacie et al., 2017).

350 **4 Results**

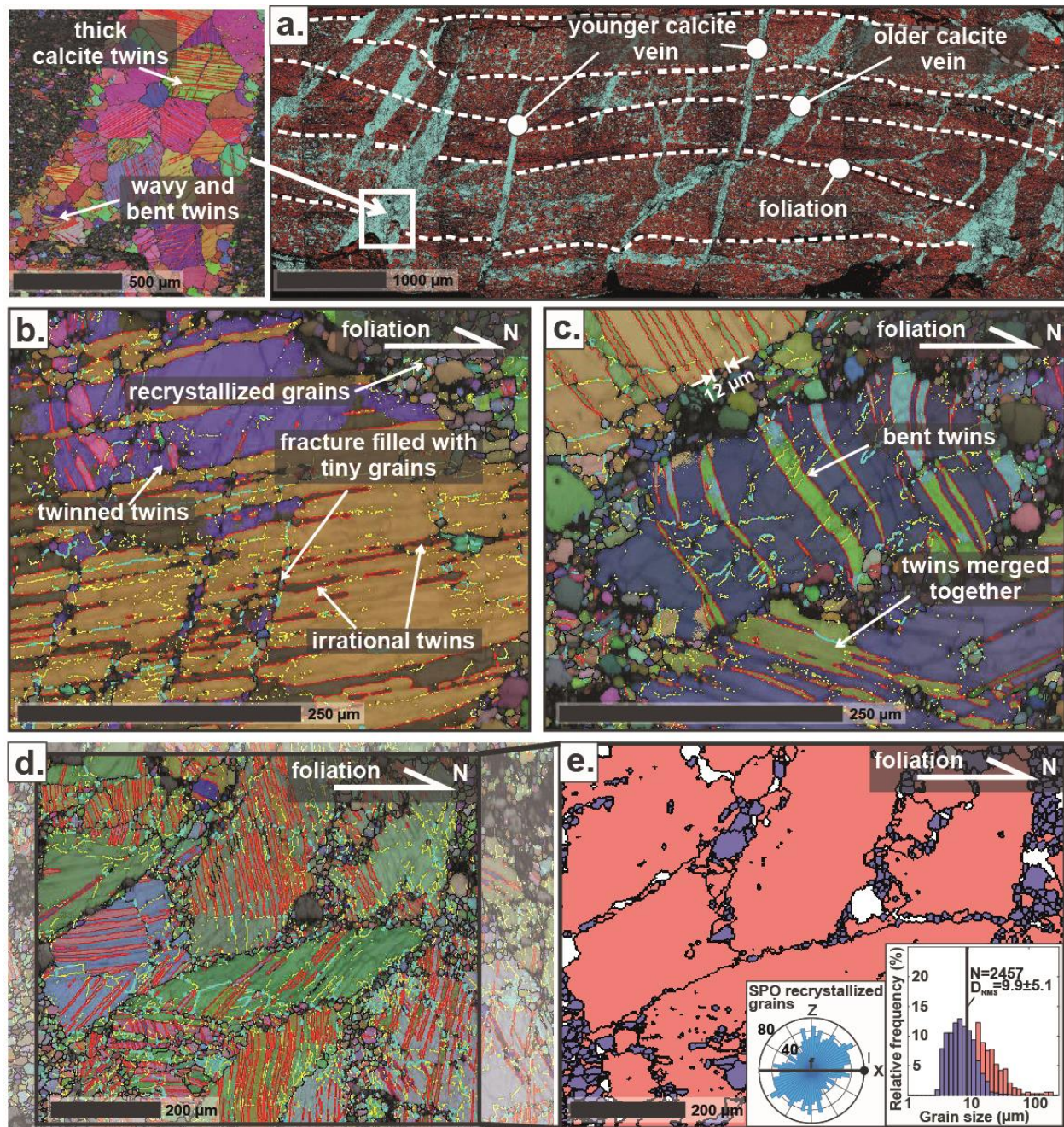
351 **4.1 Paleostresses and Deformation Temperatures Based on Calcite Veins**

352 *Field and microstructural description of the calcite veins*

353 Most calcite veins cross-cutting the mylonites and subjacent nonmylonitic schists are
 354 oriented subperpendicular to the foliation (Figure 2a). In the mylonites, some veins are disposed
 355 at shallower angles and appear to have been deformed away from that originally steep attitude as
 356 a result of top-to-the-north shearing. These latter veins are commonly cross-cut by younger, less
 357 deformed veins that remain more nearly foliation-orthogonal. Calcite veins in the mylonites
 358 usually contain large, up to 1 mm-sized (long axis of grain), twinned grains that are surrounded
 359 by fine, 5–20 μm -sized, untwinned calcite grains (“core and mantle” microstructure; Figures 2b–
 360 2e). Grain boundaries of the larger grains are usually interlobate and bulged at a wavelength that
 361 is similar to the size of the finer calcite grains (Figure 2c), suggesting dynamic recrystallization
 362 by subgrain rotation recrystallization. In two-dimensional EBSD maps, the long axes of the
 363 recrystallized grains are oriented oblique ($\sim 30^\circ$) to the mylonitic foliation (Figure 2e, inset) and

364 define a weak shape-preferred orientation (SPO). Calcite twins in the larger calcite grains are
365 thick and patchy, bent, twinned, and have sutured twin boundaries (Figures 2b and 2c). The veins
366 also contain single twin boundaries that bulge into the untwinned crystal and merge with other
367 twins within the same calcite grain. These twin morphologies resemble Type IV and Type III
368 twins of Burkhard (1993) consistent with deformation at temperatures $>250\text{--}400^\circ\text{C}$ (e.g., Evans
369 & Dunne, 1991; Ferrill et al., 2004). Some calcite veins contain $\sim 200\ \mu\text{m}$ -sized calcite grains
370 with up to $\sim 3\ \mu\text{m}$ -thick twins (Figure 2a, inset), resembling Type III and Type II twins of
371 Burkhard (1993) that may record a lower deformation temperature ($\sim 200\text{--}300^\circ\text{C}$) conditions
372 (Groshong et al., 1984; Evans & Dunne, 1991; Ferrill et al., 2004).

373

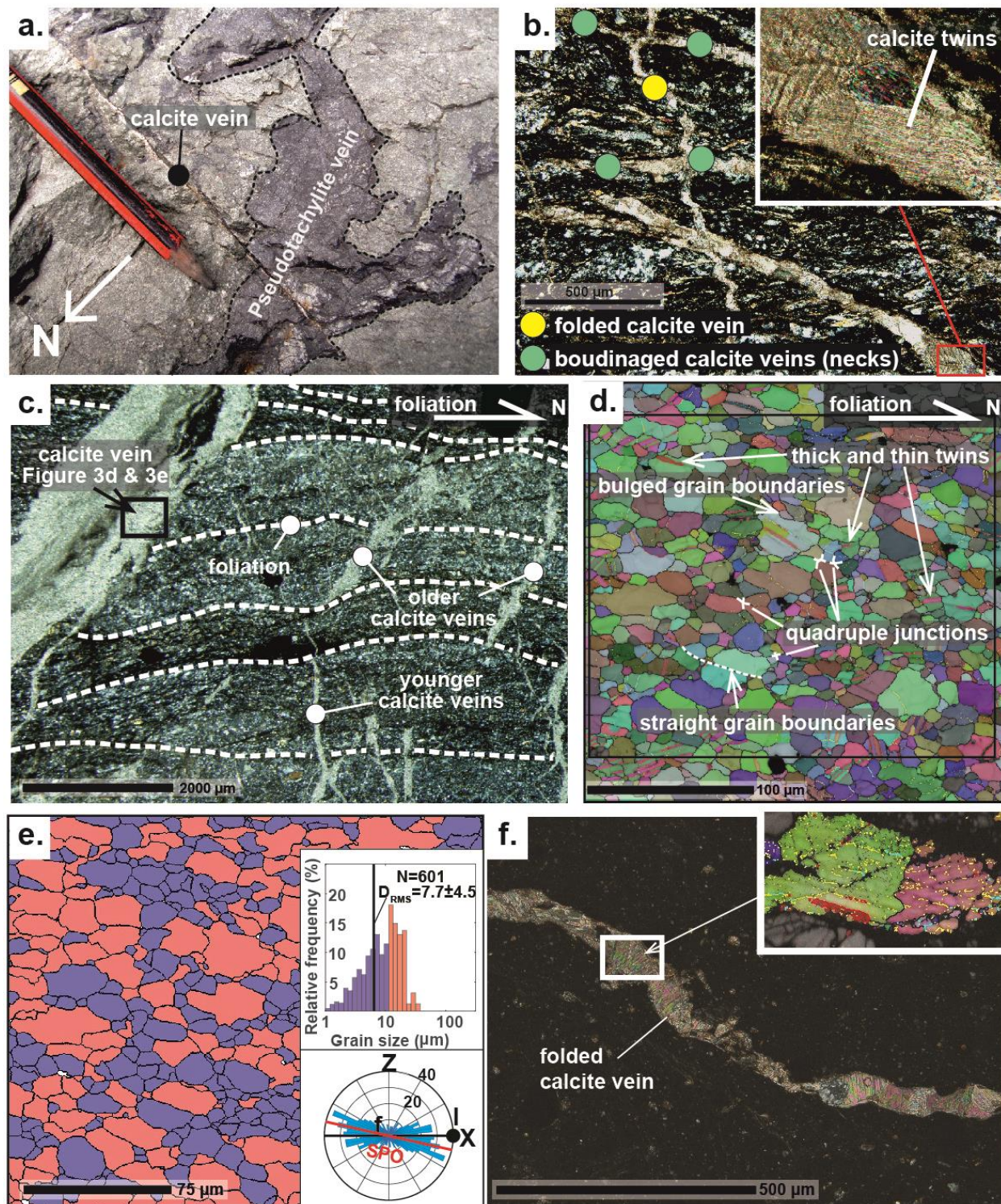


374
 375 **Figure 2.** Representative EBSD-based microstructural images of calcite veins in nonmylonitic
 376 schist (sample PNG14-15 in part a.) and in mylonite (sample PNG16-1BW in parts b. through
 377 e.). The normal (top-to-the-north) slip sense of the Mai’iu fault is shown as top-to-the-right. a)
 378 Phase map of nonmylonitic metapelitic schist from ~3 m below the fault trace, containing
 379 multiple generations of calcite veins; older, more deformed grains are oblique to the foliation
 380 (more sheared). Phases: light blue—calcite; red—quartz; white dashed lines—foliation. Inset on
 381 left: enlargement of deformed calcite vein containing twinned grains. b) All Euler color map of a

382 large (~1 mm) calcite grain surrounded by fine calcite grains. Several twins (~25 μm -wide) are
383 internally twinned. c) All Euler color map of large (~300 μm) calcite grains surrounded by fine
384 calcite grains. Large calcite grains show bent twins and twin boundaries that merge with other
385 twins in the same host grain. d) All Euler color map showing several large calcite grains with
386 thick twins and fine-grained calcite at the grain boundaries of the larger grains. e) Map of relict
387 (red) and inferred recrystallized (blue) calcite grains (area investigated shown in d.). Rose
388 diagram (inset) shows a weak recrystallized calcite grain shape-preferred orientation. Grain size
389 histogram of relict (red) and recrystallized (rex; blue) grains of map shown in e. D_{RMS} —mean
390 (root mean square) recrystallized grain size. Color code for crystallographic misorientation of
391 boundaries in a. (inset), b., c. and d. are: yellow 2–5°, light blue 5–10°, black >10° (grain
392 boundaries), red $77 \pm 5^\circ$ (twins).

393

394 The foliated cataclasites host multiple generations of calcite veins that have mutually
395 cross-cutting relationships with respect to local ultracataclasite seams and inferred
396 pseudotachylite veins (Figure 3a; see also Little et al., 2019). The calcite veins are μm - to ≤ 5 mm
397 thick and are generally oriented either suborthogonal or subparallel to the shallow (N-dipping)
398 foliation. Backward-inclined gash veins with respect to the normal sense of shear are
399 microfolded, whereas forward-inclined ones have been stretched and show necking structures, a
400 relationship attributed to normal-sense ductile shearing (Figure 3b). The calcite veins typically
401 consist of ~30–100 μm -sized, almost fully-twinned calcite grains containing predominantly
402 ~0.5–2 μm wide, straight twins (Figure 3b, inset). These resemble Type II and Type I twins of
403 Burkhard (1993), and suggest deformation temperatures of ~150–300°C (e.g., Evans & Dunne,
404 1991; Ferrill et al., 2004). Some calcite veins contain very fine-grained calcite with a grain size
405 of ~3–15 μm (Figures 3c–3e). Larger calcite grains with a grain size of ~20–50 μm have bulged
406 grain boundaries at a wavelength of ~4–12 μm and usually contain more abundant twins (~0.5–3
407 μm -wide) than the surrounding finer grains. The finer calcite grains typically form quadruple
408 grain boundary junctions as well as straight grain-boundaries with neighbouring calcite grains;
409 these grains are inferred to be recrystallized. The long axes of the recrystallized grains are
410 slightly oblique (~16°) to the spaced foliation of the foliated cataclasites and define a strong SPO
411 (Figure 3e).



412
 413 **Figure 3.** Microstructural observations of calcite veins in foliated cataclasites and
 414 ultracataclasites. Images are arranged with the top-to-the-north (normal) slip sense of the Mai'iu
 415 fault shown as top-to-the-right (except in a.). a) Fault-exhumed exposure of foliated cataclasite

416 and a pseudotachylite vein cross-cut by a mm-thick calcite vein just south (<5 m) of the active
 417 fault trace. b) Optical photomicrograph (crossed polarizers) of foliated cataclasite containing
 418 multiple calcite veins (PNG16-125B). Inset, calcite veins contain 50 to 100 μm -sized calcite
 419 grains that are almost fully twinned. Yellow dots—shortened and microfolded calcite veins;
 420 green dots—stretched calcite veins showing necking structures. c) Optical photomicrograph
 421 (crossed polarizers) showing the fine-grained mafic matrix of a foliated cataclasite cross-cut by
 422 multiple generations of calcite veins (PNG16-151E). Older calcite veins are more deformed and
 423 forward-inclined than the thinner, younger veins. White dashed lines—traces of foliation. d) All
 424 Euler angle colouring map of a calcite vein segment in foliated cataclasite (area shown in c.).
 425 Boundary misorientations are coded as follows: black $>10^\circ$ (grain boundaries), red $77^\circ \pm 5^\circ$
 426 (twins). e) Map of relict (red) and recrystallized (blue) calcite grains. Insets, top: grain-size
 427 histogram of relict (red) and recrystallized (rex; blue) grains of map d. Average grain size (root
 428 mean square; D_{RMS}) is given for the recrystallized grains; bottom: rose diagram showing a shape-
 429 preferred orientation (SPO) of recrystallized calcite grains. f) Optical photomicrograph of calcite
 430 vein in ultracataclasite (crossed polarizers). Inset, all euler angle colouring map of a calcite vein
 431 segment (same boundary misorientation coding as d.).

432

433 The ultracataclasites host $\sim 100 \mu\text{m}$ -thick calcite veinlets (Figure 3f). Backwards-inclined
 434 veinlets with respect to the shear sense of the Mai'iu fault are microfolded, whereas those which
 435 are forward-inclined are planar, like the ones described in the foliated cataclasites. The calcite
 436 veins consists of $\sim 50\text{--}100 \mu\text{m}$ -sized calcite grains that usually contain predominantly $<1 \mu\text{m}$ -thin
 437 twins (Figure 3f, inset) suggesting that deformation of these veins was mainly accommodated by
 438 twinning. The twin morphologies match the Type I twins of Burkhard (1993) and indicate
 439 deformation temperatures of $\leq 170^\circ\text{C}$ (e.g., Groshong et al., 1984; Ferrill et al., 2004).

440

441 *Estimated differential stresses and deformation temperatures*

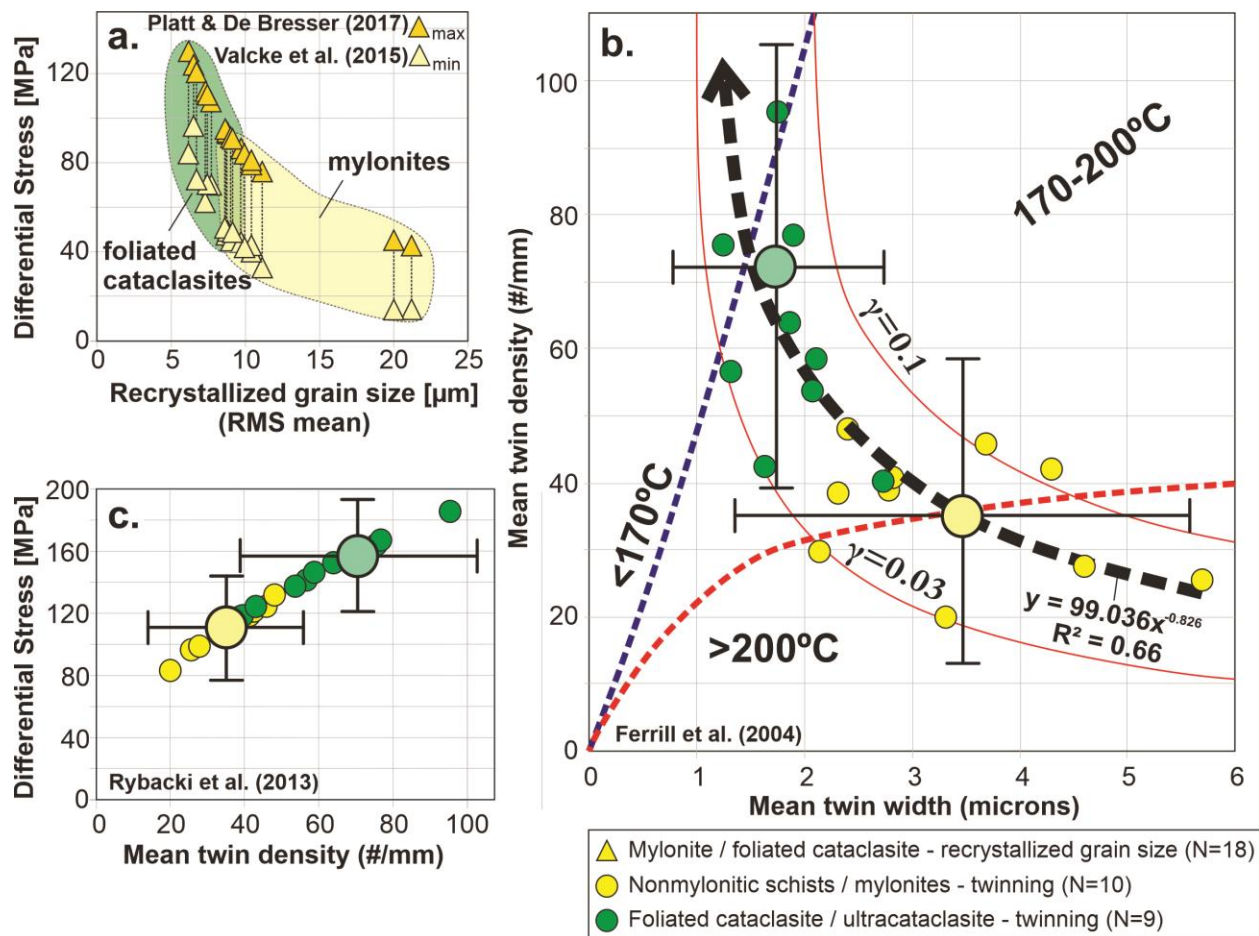
442 The grain size of recrystallized calcite in deformed veins cross-cutting the mylonites and
 443 foliated cataclasites was used to estimate differential stresses (Figure 4a). The EBSD-based
 444 estimated two-dimensional mean grain sizes (root mean square, RMS) of recrystallized calcite
 445 grains in mylonites range from $21 \pm 14 \mu\text{m}$ (N=288, 1σ ; PNG16-125D) to $9 \pm 5 \mu\text{m}$ (N=3465, 1σ ;
 446 PNG16-142C) yielding average differential stresses of $\sim 28 \pm 14 \text{ MPa}$ to $\sim 70 \pm 21 \text{ MPa}$,

447 respectively. Mean recrystallized grain sizes in the foliated cataclasites range from $9\pm 4\ \mu\text{m}$
448 ($N=892$, 1σ ; PNG16-151C) to $7\pm 4\ \mu\text{m}$ ($N=1558$, 1σ ; PNG16-17E) indicating average differential
449 stresses in that unit ranging from $\sim 68\pm 23\ \text{MPa}$ to $\sim 110\pm 14\ \text{MPa}$, respectively.

450 Calcite e-twins show a decrease in mean twin width and an increase in the mean twin
451 density as the mylonites and subjacent schists ($3.4\pm 2.2\ \mu\text{m}$ twin width, 1σ ; $\sim 36\pm 22$ twins/mm,
452 1σ) transition structurally upwards into the foliated cataclasites and ultracataclasites ($1.8\pm 1.0\ \mu\text{m}$
453 twin width, 1σ ; $\sim 72\pm 33$ twins/mm, 1σ). The estimated twin densities and the twin widths are
454 consistent with a decrease in deformation temperature from $>170^\circ\text{C}$ in the mylonites and schists
455 to $<170\text{--}200^\circ\text{C}$ in the foliated cataclasites and ultracataclasites (Figure 4b). Differential stresses
456 based on mean twin densities (Figure 4c) range between $80\text{--}135\ \text{MPa}$ (mean $110\pm 34\ \text{MPa}$) in the
457 mylonites and subjacent schists to $140\text{--}185\ \text{MPa}$ (mean $157\pm 36\ \text{MPa}$) in the foliated cataclasites
458 and ultracataclasites. Although foliated cataclasite sample PNG15-50RD yielded a high
459 differential stress estimate of $229\pm 47\ \text{MPa}$, we determined that pervasive intragranular fracturing
460 affected this estimate. Thus, sample PNG15-50RD was excluded in Figure 4.

461

462



463
 464 **Figure 4.** Estimated differential stresses and deformation temperatures of fault rocks based on
 465 calcite microstructures. a) Differential stress versus recrystallized grain size plot. b) Graph of
 466 mean twin density versus mean twin width. Dashed lines separate deformation temperature
 467 domains (after Ferrill et al., 2004). Curved red lines are isostrain magnitude contours (similar to
 468 Ferrill et al., 2004; γ —shear strain). Black arrow depicts trend of decreasing deformation
 469 temperatures in the samples representing the transition from mylonites to foliated
 470 cataclasites/ultracataclasites. Large colored circles indicate average mean twin widths and mean
 471 twin densities with average standard deviations (1σ ; black bars) of mylonites and nonmylonitic
 472 schists (yellow), and foliated cataclasites and ultracataclasites (green). c) Graph of differential
 473 stress versus mean twin density. Large circles indicate average differential stresses and mean
 474 twin densities with average standard deviations (1σ ; black bars) of mylonites and nonmylonitic
 475 schists (yellow), and foliated cataclasites and ultracataclasites (green).

476

477

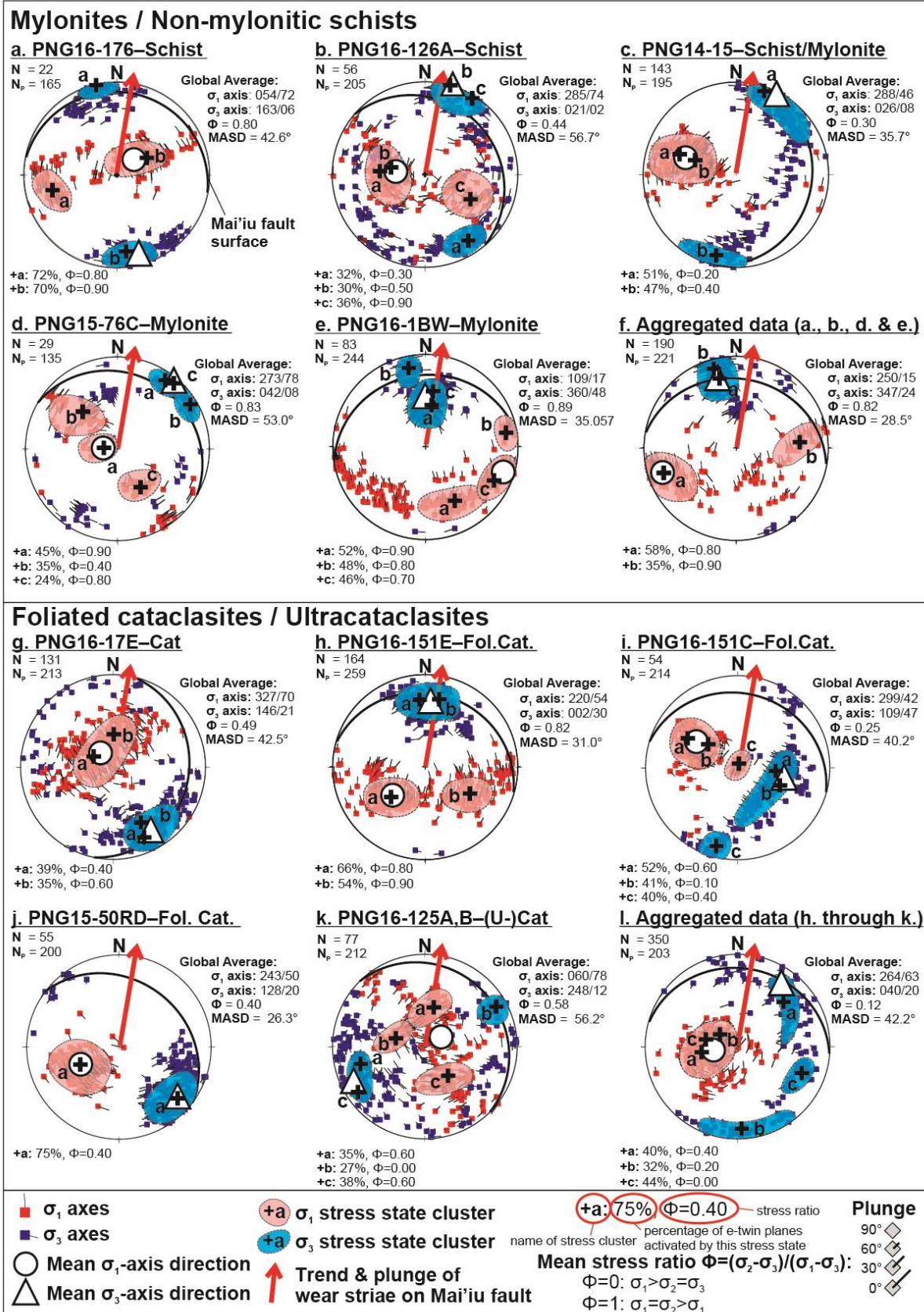
Paleo-principal stress orientations and stress ratios based on calcite-twin slip data

478 Figure 5 plots solutions for best-fit principal stress axes as calculated from subsets of the
479 calcite twin orientation data by the MIM method for veins in 10 fault rock samples. Each stress
480 solution (tadpole) for a random subset of five calcite-twin pairs ($k=5$) is represented by a σ_1 (red
481 square) and a σ_3 (blue square). The tadpole tail of each solution indicates the azimuth and plunge
482 of the opposing principal stress axis (i.e., the σ_1 -tadpole tail points in the direction of σ_3 and vice
483 versa). Clusters of σ_1 and σ_3 represent multiple solutions with similar attitudes. The densest of
484 these were manually grouped into oblong fields (to represent the clusters) that are shaded red or
485 blue, as appropriate. The percentage of the data (calcite-twin pairs) that lie within each stress
486 solution cluster (and achieve an angular misfit threshold of $<30^\circ$) is labelled below the
487 stereoplot, as is the mean stress ratio (Φ) corresponding to that cluster. For each sample, the
488 globally averaged solution for the σ_1 and σ_3 axes, spanning all of the calcite-twin pair subsets, is
489 indicated by large white circles (σ_1) and white triangles (σ_3) in each stereogram, respectively (see
490 Yamaji & Sato, 2006). For these global-average stress solutions, the mean angular dispersion of
491 the component subsets from the global average is given by the Mean Angular Stress Distance
492 (MASD)-value (Yamaji & Sato, 2006).

493

494

495



497 **Figure 5.** Reconstructed principal stress directions (lower hemisphere, equal-area stereograms)
 498 based on observed calcite-twin pairs as analysed by the MIM-method. Solutions for σ_1 (red) and
 499 σ_3 (blue) are indicated by filled squares. Red and blue shaded regions identify dense clusters of
 500 stress axis directions (σ_1 and σ_3 , respectively) that are labelled “a”, “b” and “c”. The white circles
 501 and triangles depict global average stress directions based on averaging of all the constituent data
 502 subsets. Black great circles—orientation of the Mai’iu fault surface at the respective sample
 503 location. MASD—mean angular stress distance (see text for explanation); N—Number of
 504 calcite-twin pairs; N_P —Number of stress states plotted. Sample locations are shown on Figure
 505 1b. All samples are from the footwall close to the active fault trace except 5c and 5g, which are
 506 from the footwall close to the inactive trace of the fault. Note, that the aggregated data used in
 507 parts 5f and 5l exclude data from the inactive Mai’iu fault trace veins (5c, 5g), as the fault rocks
 508 and veins beneath it, have been tilted east by up to 16° as a result of the synformal deformation
 509 on the western limb of the rider block (Figure 1b). a) PNG16-176 (nonmylonitic mafic schist). b)
 510 PNG16-126A (nonmylonitic mafic schist). c) PNG14-15 (phyllitic mylonite/schist). d) PNG15-
 511 76C (mylonite). e) PNG16-1BW-B (mylonite). f) Stress states calculated for aggregated data
 512 from all calcite vein samples (except 5c) in the mylonites and underlying schists. g) PNG16-17E
 513 (cataclasite). h) PNG16-151E (foliated cataclasite; Figure 3c). i) PNG16-151C (foliated
 514 cataclasite). j) PNG15-50RD (foliated cataclasite). k) PNG16-125A, B (foliated
 515 cataclasite/ultracataclasite). l) Stress states calculated for aggregated data from all calcite vein
 516 samples (except 5g) in the foliated cataclasites and ultracataclasites.

517

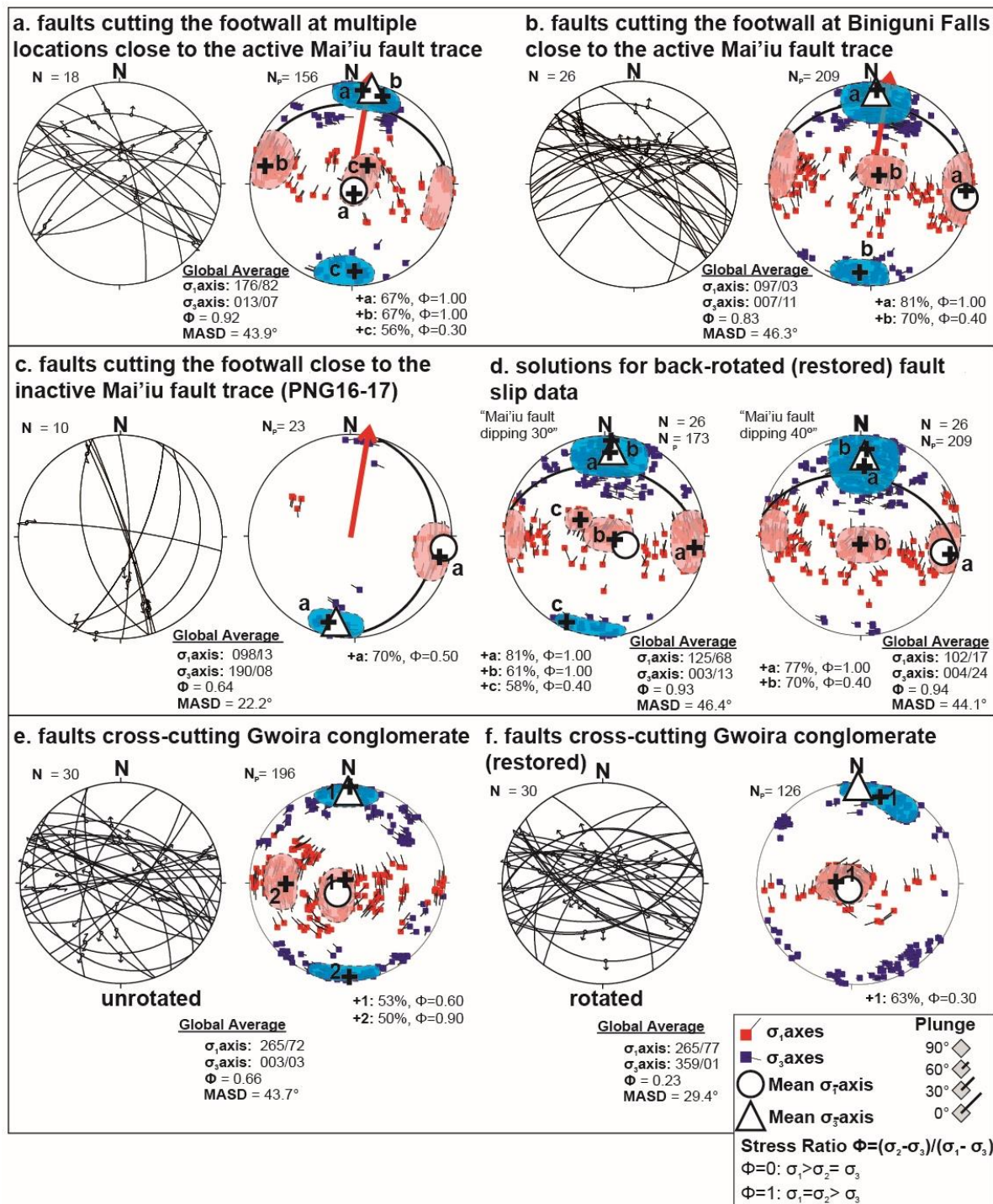
518 Based on this analysis, calcite veins in mylonites and nonmylonitic schists produce
 519 estimates for σ_1 that chiefly plunge subvertically or subhorizontally in an \sim E–W direction (i.e.,
 520 subparallel to the strike of the Mai’iu fault), and they yield estimated stress ratios (Φ) of \sim 0.30–
 521 0.89 (range of global averages). The corresponding σ_3 axes typically plunge subhorizontally in a
 522 \sim N–S direction, which is subparallel to the direction of regional extension and to the slip vector
 523 on the Mai’iu fault, with some plunging slightly more shallowly or steeply to the N than the dip
 524 of the Mai’iu fault, and others (less commonly) trending gently to the south (Figures 5a–5e).
 525 Stress directions calculated from the aggregated dataset of all calcite veins in the mylonites and
 526 nonmylonitic schists (combining datasets a.–e. in Figure 5) are shown in Figure 5f. This
 527 compiled data yields an average solution for σ_1 that plunges gently WSW (250/15) and one for

528 σ_3 that plunges NW (347/24) together with a mean stress ratio (Φ) of 0.82, indicative of a
529 constrictional stress state (i.e., $\sigma_1 \approx \sigma_2$).

530 Stress solutions derived from twin pairs in deformed calcite veins in the structurally
531 overlying foliated cataclasites and ultracataclasites are more complex and variable. They mostly
532 record σ_1 directions that populate subvertical clusters carrying stress ratios of 0.25–0.82 and σ_3
533 axes that plunge subhorizontally in ~N–S direction or at an moderate angle (~47°) towards the
534 east (Figures 5g–5k). The aggregated dataset from the foliated cataclasites and ultracataclasites
535 (combining datasets h.–k., Figure 5l) indicate an overall subvertical σ_1 direction (264/63); σ_3
536 directions are quite scattered lying on a NW-SE striking great circle with a shallow dip direction
537 towards the NE (at 040/20). The global average estimated stress ratio is low (Φ of ~0.12; i.e.,
538 $\sigma_2 \approx \sigma_3$), with individual subset solutions that are quite variable.

539 **4.2 Paleo-Principal Stress Orientations and Stress Ratios based on Fault-slip Data for Late** 540 **Brittle Faults**

541 We infer paleo-principal stress orientations based on fault-slip data measured on
542 mesoscopic (slip <1.5 m) faults cutting the footwall of the Mai'iu fault near the base of the scarp,
543 which is the most recently exhumed part of the fault surface. The analyzed fault assemblage is
544 dominated by normal faults and strike-slip faults (both dextral and sinistral). From these, we
545 derived stress solutions based on: 1) an amalgamation of most of the fault-slip data spanning
546 localities at a strike length of ~6 km to the west and ~20 km to the east of Biniguni Falls (Figure
547 6a); and 2) another large fault-slip dataset (not included in part a) that was collected at our most
548 densely studied, single field locality (Biniguni Falls, Figure 6b—for location see Figure 1d); 3)
549 fault slip data collected in the synclinal rider block, ~26 km to the east of Biniguni Falls (east-
550 tilted, inactive part of the Mai'iu fault, Figure 6c); 4) fault-slip data from Biniguni Falls locality
551 (same as part b) but analysed after attempting to restore the data for southward backtilting of the
552 footwall by 30° and 40° (inferred rolling hinge deformation, Figure 6d); and 5) fault-slip data in
553 former hangingwall strata of the Gwoira Conglomerate exposed in the rider block (using present-
554 day orientations, Figure 6e, and after an attempted back-rotation to horizontal of stratal dips,
555 Figure 6f).



556

557 **Figure 6.** Fault-slip data and calculated paleo-principal stress axis solutions based on MIM
 558 analysis for small brittle faults cutting the northernmost footwall of the Mai'iu fault (e.g., Fig.
 559 1f). a) Solutions based on all sites to the west and east of Biniguni Falls at sites PNG15-52,
 560 PNG15-76, PNG16-142, PNG15-50 and PNG16-151 (for locations, see Fig. 1b). b) Solutions
 561 based on Biniguni Falls location, PNG16-1BW (see Figs. 1b and 1d). c) Solutions based on data

562 collected beneath the abandoned and east-tilted part of the Mai'iu fault at site PNG16-17 (the
 563 rider block, see Fig. 1b). d) Same as b., but stress inversion was undertaken after an initial
 564 rotation of the fault-slip data about the local 103° strike of the Mai'iu fault to restore the Mai'iu
 565 fault (now dipping 22° NE at the surface) to an inferred former dip of 30° (stereogram on left),
 566 or of 40° (stereogram on right). e) Solutions based on present-day attitudes of the collected fault-
 567 slip data (mostly steep normal faults) cutting the Pliocene strata (Gwoira Conglomerate, former
 568 hangingwall of Mai'iu fault) in the rider block. f) Same as e., but, stress inversion was
 569 undertaken after restoring the (generally southward) dip of bedding at each data locality to
 570 horizontal by a rotation its strike. Heavy blue-colored great circles in parts a-d plot mean
 571 attitude and striae plunge for the Mai'iu fault plane at each locality.

572

573 Based on our fault-slip data for small faults cutting the footwall along the active
 574 rangefront, the calculated σ_1 axes fall into two main clusters: 1) subvertical (Figure 6a); and 2)
 575 plunging subhorizontally to the ENE or WNW; that is, subparallel to the strike of the Mai'iu
 576 fault (Figure 6b). In both cases, mean solutions for σ_3 plunge subhorizontally to the NNE. The
 577 mean stress ratios (Φ) range from 0.83 to 0.92, indicating that σ_1 and σ_2 are of subequal
 578 magnitude ($\sigma_1 \approx \sigma_2$), corresponding to a constrictional stress state. These principal stress
 579 orientations and stress ratios, based on fault-slip data, are similar to those inferred for calcite
 580 veins in mylonites and nonmylonitic schists, based on the calcite twinning analysis (Figures 5a–
 581 5f).

582 Farther east, in the rider block, mean solutions for σ_1 plunge subhorizontally to the ENE
 583 whereas those for σ_3 plunge gently to the SSW (Figure 6c). The estimated stress ratio (Φ) is 0.64.
 584 At this location, the Mai'iu fault is inactive and has been tilted $\sim 16^\circ$ east on the limb of a
 585 syncline (Little et al., 2019). Attempting to back-restore the fault-slip data to account for this late
 586 tilting does not result in a major change in the mean solutions for σ_1 and σ_3 , except that σ_1 now
 587 plunges gently towards the WNW.

588 The Mai'iu fault is known to have back-rotated (i.e., tilted southward to shallow its
 589 northerly dip) as a result of a rolling-hinge unloading process (Mizera et al., 2019; Webber et al.,
 590 2020; Watson et al., 2021). In an attempt to account for (remove) this late-stage tilting, we
 591 rotated the fault slip data at Biniguni Falls (same data as used in Figure 6b) about the local strike
 592 of the Mai'iu fault (103°) before inverting the data for best-fit stress orientations. This was done

593 in two different ways (Figure 6d): 1) by assuming that the Mai'iu fault (which today dips $\sim 22^\circ$
594 NNE at the surface at this locality) originally dipped 30° (left-hand stereogram) at the time when
595 the small-scale faults formed; and 2) by assuming that it originally dipped 40° (right-hand
596 stereogram). Regardless of the particular rotation used, the structurally restored fault-slip data
597 yields mean solutions for σ_3 that plunge N or NNE at an angle that is 11° to 17° more shallow
598 than the Mai'iu fault plane. With increasing inferred original dip of the Mai'iu fault at the time of
599 brittle fault formation (transition from Figures 6b to 6d), the reconstructed plunge of σ_3 increases
600 correspondingly (while still plunging slightly more shallowly than the fault). In all cases, mean
601 σ_1 either plunges subhorizontally to the WNW or ENE—or it is subvertical (Figures 6b and 6d).
602 Such “flipping” of σ_1 between subhorizontal and subvertical is not unexpected given the high
603 stress ratios of $\Phi=0.83\text{--}0.94$ ($\sigma_1 \approx \sigma_2$).

604 As a final exercise, we inverted fault-slip data in the former hangingwall of the Mai'iu
605 fault (southwardly back-tilted strata of the Gwoira Conglomerate in the rider block) for best-fit
606 stress directions. The analysed small-offset faults are almost entirely normal faults dipping at a
607 moderate to steep angle relative to bedding. These include a mixture of both synthetic (down-to-
608 the-north) and antithetic senses of slip. Inversion of these fault-slip data using their present-day
609 orientations yields estimates for σ_1 that vary between subvertical to subhorizontal, (E-W
610 trending, Figure 6e). The corresponding σ_3 axes plunge gently to the north or south. The global
611 average of this dataset yields a subvertical σ_1 , a N-trending, subhorizontal σ_3 and a stress ratio of
612 $\Phi=0.66$ (MASD= 44°) and is thus almost “ideally” Andersonian. Despite a diversity of measured
613 bedding and fault dips in the dataset, local bedding-fault angles everywhere remain $55\text{--}78^\circ$ —a
614 relationship that suggests that faulting predated most of the stratal tilting. To account for this, we
615 first rotated every fault-slip datum about the local strike of bedding to restore that bedding to
616 horizontal, before undertaking the stress analysis (Figure 6f). Such “unrotation” of the fault-slip
617 data results in stress solutions that are less scattered and more homogenous (mean angular stress
618 distance reduced from 44° to 29°). These solutions yield a mean trend of σ_3 that is NNE (rather
619 than NS)—a result that accords better with the known extension direction of the Mai'iu fault and
620 Woodlark rift.

621 **4.3 Calcite Clumped Isotope Paleotemperatures**

622 Clumped isotope analyses of calcite, including “conventional” oxygen and carbon isotope
623 analyses, were performed to determine the temperature of calcite precipitation in veins and rock
624 matrices and cements across the Mai’iu fault plane. The measured oxygen and carbon isotope
625 ratios and their interpretation regarding the sources of the calcite-precipitating fluids are detailed
626 in the Supporting Information S6. Clumped isotope thermometry of calcite in most samples of
627 nonmylonitic schists and mylonites (n=7) yielded temperatures of 150–200°C (Supporting
628 Information Table S6). These temperatures are well below inferred peak metamorphic
629 temperatures of the Goropu Metabasalt (425±50°C; Daczko et al., 2009) and mostly below the
630 temperature range estimated from calcite twin morphologies for calcite veins in the nonmylonitic
631 schists and mylonites (>200–300°C and 250–400°C, respectively; see above). Thus, apart from
632 perhaps the highest clumped isotope-based paleotemperatures—236±41°C and 223±12°C (for
633 mylonite sample PNG15-52A)—the clumped isotope-based paleotemperatures for calcite veins
634 in schist and mylonite samples do not document the crystallization temperatures of calcite.
635 Rather, these probably represent blocking of isotope reordering in calcite during later
636 exhumational cooling of the footwall, as has been shown for calcite marbles in other
637 metamorphic core complexes (e.g., Stolper & Eiler, 2015; Ryb et al., 2017).

638 By contrast, calcite veins in the foliated cataclasites and ultracataclasites (n= 4) yield
639 temperatures estimates ranging from 130±8°C to 160±14°C, mostly below calcite blocking
640 temperatures, and thus may record original temperatures of calcite precipitation or
641 recrystallization. Significant dynamic recrystallization of calcite veins in cataclasite sample
642 PNG15-151 is indicated by EBSD imaging (Figures 3d and 3e). Recrystallization textures are
643 observed primarily in older and more deformed, forward-inclined veins; these record mean
644 paleotemperatures of ~160°C, whereas younger, thinner (and less deformed) foliation-
645 perpendicular veins record a mean paleo-temperature of ~130° (Supporting Information Table
646 S6). This temperature range (160-130°C) may bracket the interval between the minimum
647 temperature of dynamic recrystallization of calcite (Ryb et al., 2017) and complete cessation of
648 internal deformation of the cataclasites. Clumped isotope analyses of calcite cement (n=2) in the
649 Gwoira Conglomerate of the hangingwall (sample PNG16-99, Figure 1b) yielded formation
650 temperatures of 30±11°C and 32±12°C consistent with shallow burial of the conglomerate at the
651 time of cementation.

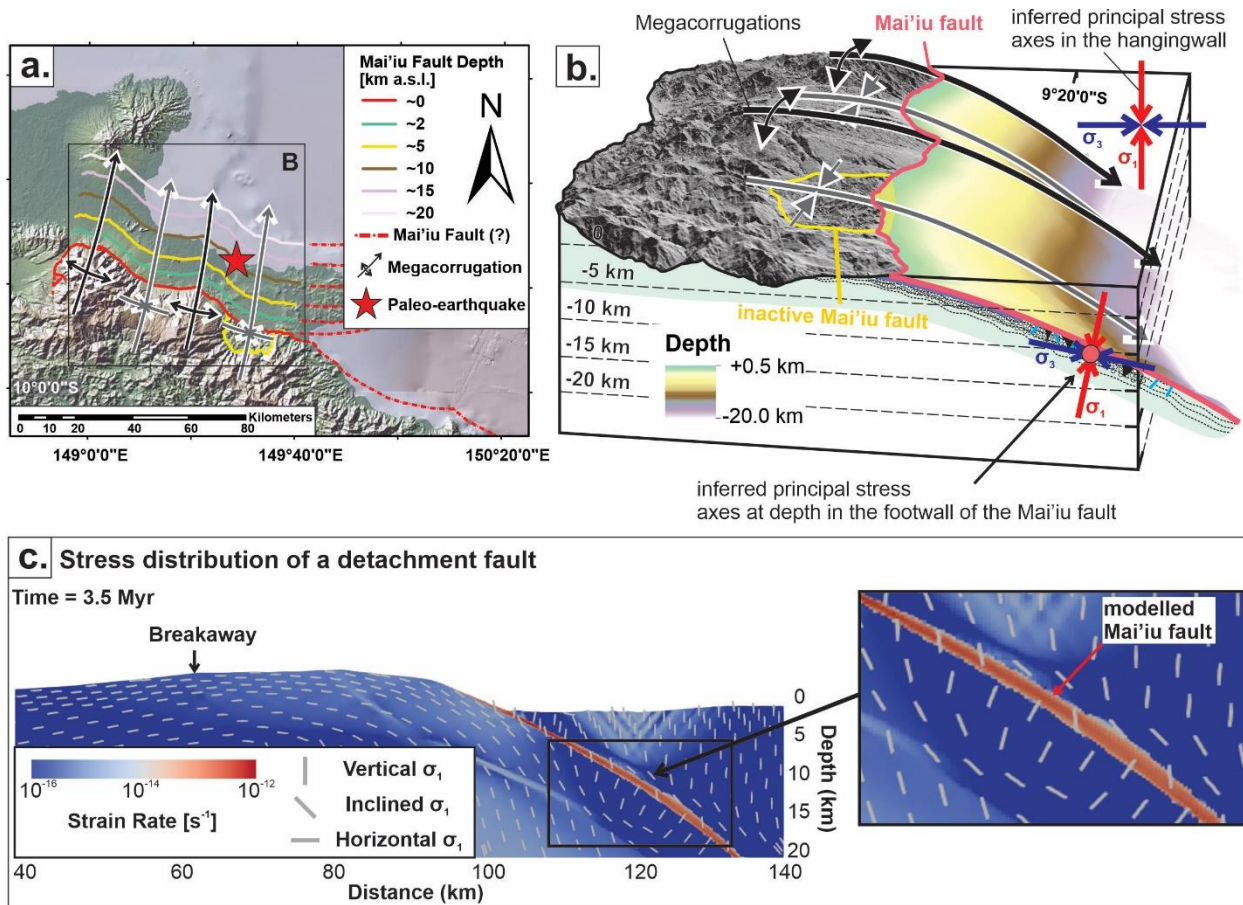
652 5 Discussion

653 5.1 Disposition of Principal Stress Axes

654 Solutions for paleo-principal stress axes based on 1) twinning of calcite veins in footwall
655 mylonites and adjacent nonmylonitic schists (Figures 5a–5f), and 2) on attitudes of small-offset
656 brittle faults cutting the exhumed footwall (mylonites and cataclasites) of the Mai’iu fault
657 (Figures 6a–6d) similarly indicate a stress state in which $\sigma_1 \approx \sigma_2 > \sigma_3$ ($\Phi \approx 0.64–0.94$; constrictional
658 state of stress), and for which σ_3 plunges subhorizontally to the ~NNE or SSW (i.e., subparallel
659 to the regional extension direction). In these solutions, σ_1 either plunges subhorizontally to the
660 ESE or WNW (subparallel to the strike of the Mai’iu fault), or is subvertical (classic
661 Andersonian extensional state of stress). Such apparent “flipping” of σ_1 in an otherwise
662 Andersonian extensional stress state agrees with several previous field studies near ancient
663 detachment faults that similarly inferred that σ_1 was either subvertical or arranged at a high angle
664 ($55^\circ–80^\circ$) to the low-angle detachment fault (e.g., Axen & Selverstone, 1994; Hayman et al.,
665 2003; Axen, 2004, and references therein). In these cited studies, principal stress orientations
666 were inferred from the attitude of mixed-mode extensional and shear fractures in the footwall
667 and/or hangingwall of the detachment.

668 In the footwall of a major detachment fault, a constrictional state of stress ($\sigma_1 \approx \sigma_2$) may
669 reflect reduction of subvertical stresses (caused by tectonic denudation from extensional fault
670 slip and/or thinning of the hangingwall) coupled with an increase in strike-parallel horizontal
671 stress during that denudation. The latter might be attributed to bending stresses in the extracted
672 footwall, which is back-flexed during its exhumation (Fletcher et al., 1995; Singleton, 2013).
673 During rolling-hinge-style flexural unbending of an exhumed footwall, the outer surface of this
674 footwall contracts in the dip direction. At the same time, the footwall stretches and thickens at
675 right angles to this. If the footwall is laterally confined parallel to fault strike (i.e., it is restricted
676 by surrounding rocks), then the footwall cannot expand in this direction. This may lead to a syn-
677 exhumational increase in strike-parallel compressive stress during fault slip, and thus to an
678 increase in σ_2 magnitude. Such a constrictional state of stress might explain the common
679 observation of extension-perpendicular shortening (and associated folding) as documented in the
680 Buckskin-Rawhide MCC, west central Arizona, (e.g., Singleton, 2013); and indeed along the
681 Mai’iu fault, where slip-parallel megacorrugations have been amplified in the near-surface as

682 active folds (Figures 7a and 7b; Little et al., 2019; Mizera et al., 2019). This model might explain
 683 the high Φ -ratio ($\sigma_1 \approx \sigma_2$) and locally \sim E–W trending σ_1 direction that we measured in the
 684 footwall of the Mai’iu fault (Figures 5a–5f and 6a–6d).
 685



686
 687 **Figure 7.** Inferred principal stress directions near the Mai’iu fault. a) Landsat image (30 m cell
 688 size) draped over Shuttle Radar Topography Mission digital elevation model (\sim 30 m cell size)
 689 showing the Suckling-Dayman Metamorphic Core Complex (SDMCC) and megacorrugations
 690 (black arrows). Red line—trace of the Mai’iu fault; yellow line—trace of the inactive Mai’iu
 691 fault; coloured lines—inferred subsurface continuation of the Mai’iu fault after Abers et al.
 692 (2016); red star—inferred formational depth of pseudotachylite veins (based on $^{40}\text{Ar}/^{39}\text{Ar}$ ages
 693 from Little et al., 2019). b) Perspective view illustrating the corrugated fault surface of the
 694 Mai’iu fault and its subsurface continuation. Principal stress axes σ_1 (red arrows) and σ_3 (blue
 695 arrows) are based on Figure 6d (footwall) and Figure 6f (hangingwall). The red dot in the middle
 696 of the footwall stress axes indicates that σ_1 and σ_2 are there of subequal magnitude (bending

697 stresses). c) Thermomechanical model from Biemiller et al. (2019) using boundary conditions
698 and rheological parameters tuned to the SDMCC. White glyphs— σ_1 -orientations (see text).

699

700 The Mai'iu fault dips $\sim 22 \pm 2^\circ$ NNE at the surface (Figure 1b, inset). Most of our fault-slip
701 data-based solutions for the orientation of σ_3 either trend to the NNE and are subhorizontal; or
702 they plunge NNE or N at an angle that is less steep than the Mai'iu fault by $10\text{--}20^\circ$. Most
703 commonly, σ_1 is subvertical (Figures 6a–6d, 7b). Poles to calcite extension gashes can be
704 interpreted as recording the σ_3 direction. Except where they have been later strongly sheared,
705 these are mostly disposed at an angle of $\sim 18\text{--}22^\circ$ to the Mai'iu fault surface (Figure 1b, inset).
706 Such Andersonian to “near-Andersonian” (i.e., slightly inclined) stress directions are
707 unfavourable for slip on the shallow-dipping (at the surface) Mai'iu fault. If the apparent non-
708 zero plunge of σ_3 is real (i.e., Figure 6d) then the stresses were not exactly Andersonian, and σ_3
709 was at a small angle to the slip direction, a situation that would make slip on the fault even more
710 mechanically unfavourable than for an exactly Andersonian stress disposition. Such stress
711 obliquity is also implied by some of our calcite-twinning based solutions for stress orientation
712 (i.e., Figures 5e and 5h). A possible cause for local departures from Andersonian stress
713 orientation might be stress concentrations around geometric irregularities or asperities in the fault
714 zone (Chester & Fletcher, 1997; Chester & Chester, 2000; Rutter et al., 2007); however, near the
715 Mai'iu fault the pattern seems to be manifested across our entire dataset.

716 Figure 7c shows stress trajectories calculated as part of a geodynamic model exploring
717 reactivation of subduction thrusts as extensional detachments (see Mizera et al., 2019 and
718 Biemiller et al., 2019 for a detailed explanation of the model). This finite element model imposes
719 extensional velocity boundary conditions across a pre-weakened subduction zone, with the white
720 glyphs depicting trajectories of σ_1 . The model reproduces a rolling-hinge evolution of the
721 detachment fault, with the exhumed portion becoming convex upward with continued extension.
722 The model is of interest here because it predicts spatial changes in stress orientation across the
723 Mai'iu fault. In the hangingwall of the fault, σ_1 is mostly vertical, but it deflects slightly
724 anticlockwise in proximity to the weak fault zone to become more nearly parallel to it. By
725 contrast, in the immediate footwall of the detachment, σ_1 deflects from the vertical in the
726 opposite sense to become more nearly perpendicular to the fault—with σ_3 arranged at a small
727 angle to the fault. At structurally higher footwall levels, adjacent to the fault, σ_1 deflects

728 anticlockwise to become more nearly Andersonian. In the model, the above-mentioned stress
729 refractions in the footwall of the model reflect flexural stresses there, and they depend on the
730 relative strengths of the footwall, the fault zone and the hangingwall materials. To what extent
731 bending stresses affected the observed orientation of stress axes in our study cannot be answered,
732 and the uncertainties in the calculated stress orientations are large. Nonetheless, the general state
733 of footwall stress that we infer ($\sigma_1 \approx \sigma_2$; σ_1 subvertical, and σ_3 subhorizontal or plunging to the
734 north at a small angle to the fault) accord with the predictions of this mechanical model.

735 In the foliated cataclasite and ultracataclasite units of the footwall, our calculated stress
736 ratios (Φ) and principal stress directions similarly indicate a mostly subvertical σ_1 , but the
737 corresponding σ_3 axes trend and plunge variably (Figures 5g–5l). The high differential stresses
738 estimated from twin densities in some of these veins (Figure 4c), and the occurrence of
739 pseudotachylites in these fault rocks (Figures 1g and 3a) suggest that the locally high inferred
740 differential stresses and variable stress orientations may reflect heterogeneous dynamic stress
741 conditions related to seismic-cycle stress reorientations (e.g., see Figure 4 in Di Toro et al., 2005;
742 Mello et al., 2010). In addition, processes like fragmentation and clast rotation after vein
743 emplacement, inelastic bending around irregularities and/or local stress concentrations around
744 asperities may have caused a deformational dispersion of twin orientations in the brittle fault
745 rocks (e.g., Rutter et al., 2007).

746 **5.2 Calcite Vein Formation and Deformation Temperatures**

747 We can assign approximate deformation temperatures to fault rocks using microstructural
748 observations of deformed calcite veins contained within them (Figure 4b; Supporting
749 Information Table S7). Calcite veins in the mylonites and subjacent nonmylonitic schists contain
750 recrystallized grains and mostly Type III and Type IV e-twins, suggesting deformational
751 temperatures of 200–400°C (Burkhard, 1993). Calcite veins in the foliated cataclasites and
752 ultracataclasites contain mostly Type II and Type I e-twins, suggesting deformation temperatures
753 <200°C (Figure 4b). Previously published chlorite geothermometry data in mylonites and
754 foliated cataclasites provide further constraints on emplacement temperature of the analysed
755 calcite vein samples in this study (potentially deformation temperatures; Supporting Information
756 Table S7; see also Mizera et al., 2020). The latter emplacement temperature estimates are based
757 on the composition of chlorite grains occupying syntectonic microstructural sites, or less

758 deformed veins cross-cutting such microstructures. Based on these results, the emplacement and
759 inferred deformation temperatures of these calcite veins are bracketed to 150–350°C.

760 The estimated apparent formation temperatures of calcite veins in mylonites and
761 nonmylonitic schists obtained from clumped-isotope geothermometry (~150–200°C) are
762 consistently lower by 50–100°C than those based on either the microstructural observations or
763 the chlorite-based paleotemperatures for corresponding rocks (Supporting Information Table S7).
764 We infer that the clumped-isotope temperatures do not record the temperature at which calcite
765 precipitated in the veins, but the temperature at which isotope reordering was blocked during
766 later cooling of the exhuming footwall (Passey & Henkes, 2012; Stolper & Eiler, 2015).
767 Furthermore, dynamic recrystallization can reset the Δ_{47} values of calcite due to efficient
768 mobilization of carbonate ion-groups during dislocation glide along crystallographic planes (Ryb
769 et al., 2017). Consequently, we interpret the clumped-isotope geothermometer-estimated
770 temperatures of (recrystallized) calcite veins in the mylonites and schists as providing a
771 minimum temperature of dynamic recrystallization (Ryb et al., 2017). In the structurally higher
772 foliated cataclasites and ultracataclasites, the clumped-isotope geothermometer is preferred
773 because chlorite-based temperatures in these rocks are inadequate due to a preferred growth of
774 corrensite (mixed layer chlorite and saponite) instead of chlorite at low temperatures (e.g.,
775 Bevins et al., 1991), and because e-twin based deformation temperatures are imprecise.

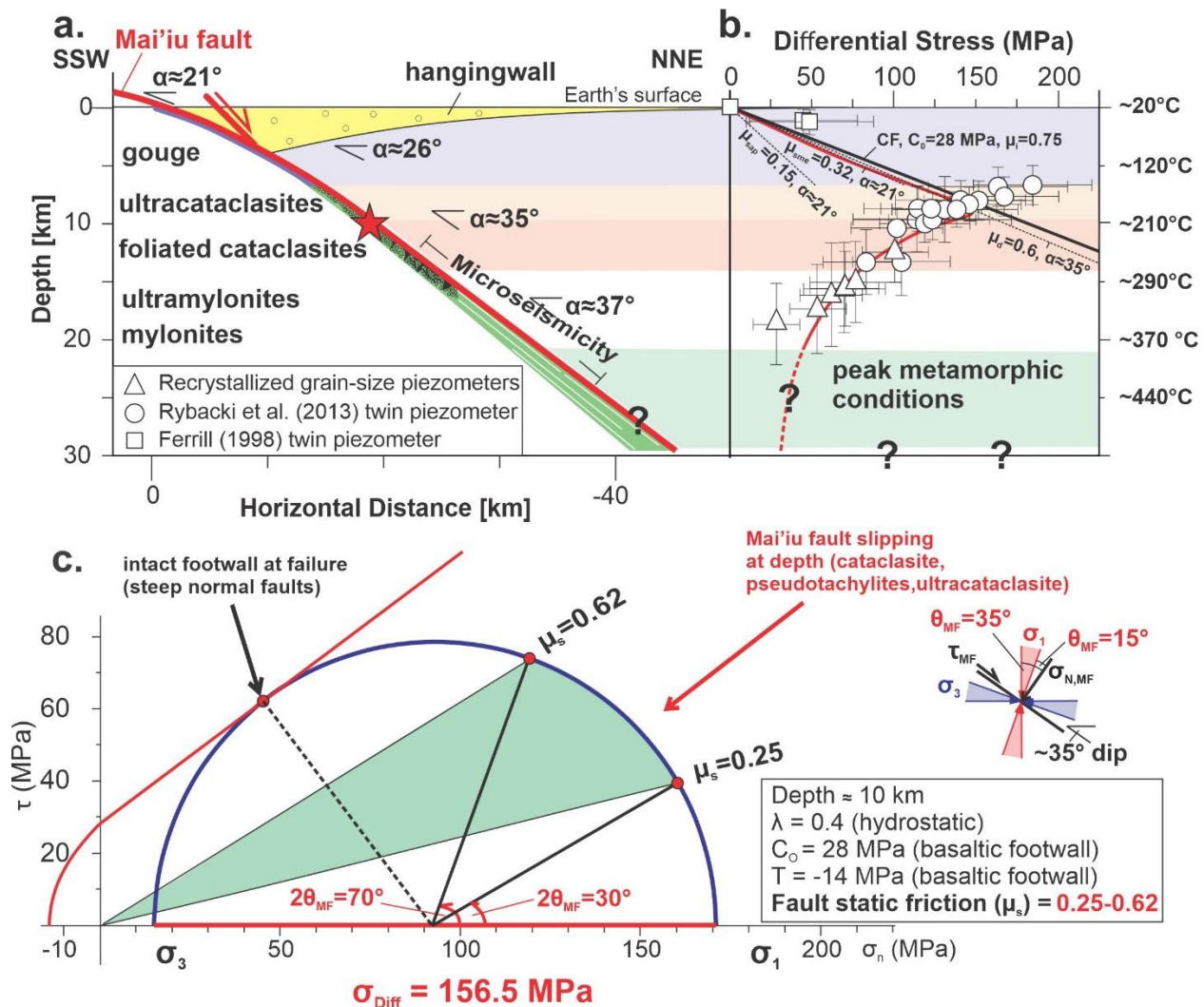
776 In summary, we used a combination of different geothermometers to bracket
777 temperatures at which calcite precipitated and deformed in the suite of fault rocks. All
778 geothermometers and paleopiezometers applied in this study show a similar trend of increasing
779 temperature and decreasing stress with increasing formational depth of the fault rock unit
780 (Supporting Information S7). In summary, (a) calcite veins in mylonite and nonmylonitic schist
781 experienced differential stresses of ~28–135 MPa at temperatures ~200–400°C, and (b) calcite
782 veins in foliated cataclasites and ultracataclasites experienced differential stresses of ~68–185
783 MPa at temperatures 130–250°C. To assign these temperature constraints to a relevant depth on
784 the Mai'iu fault requires knowledge of the variation in local geothermal gradient near that
785 structure. The local geothermal gradient has been estimated to be as high as ~24°C/km (average
786 $22 \pm 2^\circ/\text{km}$) in the upper 10 km, decreasing to ~14–16°C/km at >20 km depth based on a
787 combination of fault-proximal geological and thermochronological data (Daczko et al., 2009;
788 Österle, 2019; Little et al., 2019; Mizera et al., 2020), far-field drillhole temperatures and

789 regional heat flow data for the Woodlark Rift (Tjhin, 1976; Martinez et al., 2001), and
790 thermomechanical modelling of the fault at the relevant slip rate (Biemiller et al., 2019, 2020)
791 (see Supporting Information S8).

792 **5.3 Strength-Depth Profile of the Mai'iu fault**

793 Figure 8a is a schematic profile across the Suckling-Dayman Metamorphic Core
794 Complex showing inferred formational depths of key fault rock units in the footwall of the
795 Mai'iu fault and associated temperatures (Little et al., 2019; Mizera et al., 2020). The depicted
796 dip of the Mai'iu fault at the ground surface (21°) is that seen in outcrop along the profile in
797 Figure 1c (Mizera et al., 2019). Dip angles in the subsurface are constrained by microseismicity
798 foci at ~12–25 km depth that are colinear with the trace of the Mai'iu fault (based on a projection
799 of the microseismicity data ~40 km farther east of this profile as located by Abers et al., 2016).
800 The inferred depth at which the dated pseudotachylite veins formed (~9–16 km depth; Little et
801 al., 2019) is indicated by a red star.

802



803

804 **Figure 8.** a) Depth profile of the Mai'iu fault (modified after Little et al., 2019; Mizera et al.,
 805 2019). Microseismicity based on Abers et al. (2016). α —dip angle of the Mai'iu fault; Red
 806 Star—formational depth of dated pseudotachylite veins. b) Differential stress versus depth-
 807 temperature profile based on this study (Figure 4). The temperature-depth relationship used here
 808 is outlined in Supporting Information S8 (inferred non-steady state geothermal structure). Brittle
 809 failure curves for intact basaltic crust for which a linear Coulomb criteria (CF) limits differential
 810 stress (this assumes a footwall cohesion, C_0 , of 28 MPa, Schultz, 1993; and coefficient of
 811 friction, μ_i , of 0.75). The lines through the origin depict a non-optimally oriented, cohesionless
 812 fault with varying dip angles (α) and coefficient of frictions, for which reshear criteria limits
 813 differential stress ($\mu_{sap,sme,d} = 0.15-0.6$; dip angle of the fault, $\alpha = 21-35^\circ$). μ_{sap} —coefficient of
 814 friction for saponite (e.g., Lockner et al., 2011); μ_{sme} —coefficient of friction for smectite (e.g.,

815 Morrow et al., 2017); μ_d —“Byerlee” friction (Byerlee, 1978); red line—inferred change in
816 strength of the Mai’iu fault with depth and temperature. c) Mohr circle depicting state of stress at
817 10 km depth near the Mai’iu fault. Assumes a static friction in the footwall (μ_s) of 0.75 and
818 hydrostatic pore fluid pressure ratio of ($\lambda=0.4$) under variably Andersonian (vertical σ_1) to
819 slightly non-Andersonian stress (σ_1 plunging steeply south at 70°) regime (based on calcite veins
820 and late brittle faults in the footwall of the Mai’iu fault). To allow reshearing on the misoriented
821 Mai’iu fault (here dipping 35° , see part a), the coefficient of sliding friction on the fault (μ_s) must
822 be less than 0.6 (bottom end of “Byerlee” friction; Byerlee, 1978). For reference, a failure line
823 for $\mu_s = 0.24$ is also shown (corresponding to a smectite-rich gouge; e.g., Biemiller et al., 2020).
824 Note that even for $\mu_s = 0.6$, a differential stress of ~ 157 MPa would drive both reshear on the
825 Mai’iu fault and brittle yielding of its metabasaltic footwall.

826

827 In Figure 8b, we plot differential stresses versus depth based on our calcite
828 paleopiezometric studies (Figures 4a, 4c), and the estimated deformation temperatures of the
829 calcite veins (Figure 4b; Supporting Information S6 and S7), with these temperatures being
830 converted to depths using an estimate of the thermal structure that is presented in Supporting
831 Information S8 (including Figure S8). The error bars on each differential stress data point
832 accommodate: a) the standard deviation (1σ) of the mean twin density in the analysed calcite
833 grains (Figure 4c); b) the deviation between the Valcke et al. (2015) and Platt and De Bresser
834 (2017) recrystallized grain-size paleopiezometer (Figure 4a); c) the uncertainties in deformation
835 temperatures (vertical bars; Supporting Information Table S7); and d) the uncertainties in
836 geothermal gradient (Supporting Information S8). In Figure 8b several brittle failure curves are
837 depicted in the strength-depth profile assuming Andersonian stresses (σ_1 is vertical) and a
838 hydrostatic pore fluid pressure ratio ($\lambda=0.4$). The thick black failure curve represents failure of
839 intact basaltic crust for which a linear Coulomb Failure criteria (CF) limits differential stress
840 (cohesion, $C_0=28$ MPa, Schultz, 1993; coefficient of friction, $\mu_i=0.75$), and in which faults are
841 ideally oriented. The several dotted curves represent reshear conditions for non-optimally
842 oriented, cohesionless faults at dips (α) of 21° or 35° ; and at static coefficients of friction (μ_d) of
843 0.15, 0.32, or 0.6. The equations for the brittle failure curves and material parameters used in this
844 plot are presented in Supporting Information S10.

845 According to this profile (Figure 8b), calcite veins in the mylonites formed at depths of
846 20–12 km depth, and experienced differential stresses of 25–135 MPa, with the average stress
847 magnitude increasing with decreased temperature and depth. A peak in differential stress at ~6–
848 12 km depth was measured in calcite veins from the foliated cataclasites, which hosts
849 ultracataclasite bands and pseudotachylite veins. There, we measured some differential stresses
850 >150 MPa—a value that exceeds the theoretical brittle strength curve for intact basaltic rocks
851 (CF). This is in accordance with our observation that newly formed brittle faults cut the
852 metabasaltic footwall of the Mai'iu fault (e.g., Figures 1f and 1g). Despite this localized yielding
853 in the footwall, the Mai'iu fault as a whole remains viable—and its continued slip eventually led
854 to exhumation of its (mesoscopically faulted) footwall. Given the large differential stresses near
855 the stress peak at ~6–12 km depth, such reshear would have been possible for any coefficient of
856 friction <0.6 if the mean dip of the fault at this depth is ~35° (Figure 8b).

857 At shallower depths of <6 km, where the fault dips ~21°, the fault strength is controlled
858 by the frictional properties of the clay-rich fault gouge. Abundant saponite and corrensite were
859 identified in Mai'iu fault gouges by XRD-analysis on parts of the fault, both active and inactive,
860 that dip <21° (sites PNG16-142 and PNG16-17, Little et al., 2019; Mizera et al., 2020; Biemiller
861 et al., 2020). We infer from the known stability range of saponite ($T < \sim 150^\circ\text{C}$; e.g., Lockner et
862 al., 2011), that the saponitic gouges formed at shallow depths (<6 km) by pervasive alteration of
863 the mafic footwall (Mizera et al., 2020), thus forming a frictionally weak rock that is also prone
864 to aseismic creep (velocity-strengthening behaviour; Biemiller et al., 2020). There, we consider
865 reshear criteria appropriate to a saturated saponite- or smectite-rich fault gouge ($\mu_{\text{sap}} \approx 0.15$,
866 $\mu_{\text{sme}} \approx 0.32$; Lockner et al., 2011; Morrow et al., 2017; Biemiller et al., 2020). Figure 8b shows
867 that the differential stresses required for the fault to slip at this shallower and more misoriented
868 dip angle depend on the fault friction coefficient. The maximum allowable friction coefficient on
869 the Mai'iu fault would be that corresponding to a differential stress (for reshearing) that is equal
870 in magnitude to that required for intact fracture of the footwall by ideally oriented faults (CF
871 failure line). For a Mai'iu fault dip of 21°, this friction coefficient is ~0.38. For an active fault
872 dip that is locally as low as 16° the maximum allowable coefficient of friction would be ~0.28,
873 coincident with the maximum coefficient of friction reported for Mai'iu fault saponite-rich
874 gouges (Biemiller et al., 2020). We note that the brittle failure curves presented here assume

875 Andersonian stresses; however, our results suggest that the principal stress axes may not be
876 strictly Andersonian in the footwall of the Mai'iu fault (see above).

877 **5.4 State of Stress at Depth on the Mai'iu Fault**

878 Twinning-based differential stress estimates in the foliated cataclasites and
879 ultracataclasites (140–185 MPa; which formed at temperatures ~130–275°C, Mizera et al., 2020)
880 are interpreted to record those present at our inferred mid-crustal differential stress peak at 6–12
881 km depth (Little et al., 2019). The degree to which these stress estimates may reflect interseismic
882 stresses rather than short-lived, dynamic ones during earthquakes is uncertain. Pseudotachylite
883 veins injected into the foliated cataclasites (Figures 1g and 3a), and solutions for stress
884 orientations in those rocks that are complex and heterogeneous (Figures 5g–5k) suggest that at
885 least some of our differential stress estimates—presumably the highest ones—may reflect
886 dynamic stresses during the earthquake cycle. We have estimated a mean differential stress
887 (σ_{Diff}) for the foliated cataclasites and ultracataclasites of $\sim 157 \pm 36$ MPa (Figure 4c). Assuming
888 that this mean value is representative of the long-term, interseismic peak strength on the Mai'iu
889 fault at ~10 km depth, we can construct a Mohr circle diagram to depict this situation (Figure
890 8c). To do so, we allow σ_1 to range between vertical (ideal Andersonian stress state, σ_1 at a 55°
891 angle to the 35°-dipping fault) to slightly inclined (i.e., non-Andersonian, with σ_1 disposed at
892 ~75° to the 35°-dipping fault). We note that calcite veins in the fault rocks may indicate fluid
893 pressures sufficiently high at times to induce local hydrofracturing (i.e., $P_f > \sigma_3$); however, fluid
894 influx was not high enough to completely retrogress the metabasaltic mineral assemblage as
895 observed in other MCCs such as the Moresby Seamount Detachment in the eastern Woodlark
896 Rift (cf. Speckbacher et al., 2012, 2013). Overall, there is little evidence for sustained fluid flow
897 or high pore fluid pressure in the foliated cataclasites, which contains ductilely sheared calcite
898 veins (e.g., Figures 3b and 3c; Mizera et al., 2020). Thus, we assign pore fluid pressure ratio of
899 $\lambda=0.4$ (hydrostatic). Assuming a 35° dipping Mai'iu fault in the subsurface, our paleo-differential
900 stress measurements indicate that to drive slip on such a fault the mean coefficient of static
901 friction must have been ~0.25–0.62 in the foliated cataclasites. At times, differential stresses
902 must have been high enough (>150 MPa) to cause new brittle yielding of formerly intact, strong
903 mafic footwall rocks, as is expressed by small faults cutting the exhumed fault surface (Figures
904 1f and 1g).

905 6 Conclusions

906 Our study documents differential stresses, principal stress orientations, and temperatures
907 occurring near the active Mai'iu low-angle normal fault which has self-exhumed a sequence of
908 fault rocks that formed as the footwall was carried up through the mid crust to the surface. We
909 have applied paleostress and geothermometry analyses to the exhumed metabasaltic footwall
910 rocks and to conglomerates in the Gwoira rider block (former hangingwall) to reconstruct a
911 strength-profile through the middle crust in this region. Our results show that:

- 912 • Solutions for the orientation of σ_1 and high stress ratios (Φ) of >0.8 reflect σ_1 and σ_2 that
913 were subequal in magnitude, with significant compression subparallel to the strike of the
914 Mai'iu fault. We attribute this to a combination of vertical unloading as a result of finite
915 dip-slip on the fault together with 3-D bending stresses related to rolling-hinge style
916 flexure of the footwall.
- 917 • Differential stresses in the deepest formed mylonites and nonmylonitic schists in the
918 footwall of the Mai'iu fault ranged from >25 MPa at ~ 18 km depth up to 135 MPa at ~ 12
919 km depth.
- 920 • In the foliated cataclasites and ultracataclasites, peak differential stresses reached ~ 140 –
921 185 MPa (mean 157 ± 36 MPa) at 6–12 km depth. The high differential stresses and the
922 heterogeneity of stress solutions in these fault rocks were found to coincide with the
923 occurrence of pseudotachylite veins at this depth cross-cutting the foliated cataclasites;
924 thus suggesting that at least some of our stress estimates may reflect dynamic stresses
925 during the earthquake cycle.
- 926 • The differential stresses supported by the mid-crustal foliated cataclasites were at times
927 high enough (>150 MPa) to cause new brittle yielding of strong, formerly intact mafic
928 footwall rocks and to drive slip on a moderately dipping part of the Mai'iu fault that was
929 relatively strong.
- 930 • At the shallowest crustal levels (<6 km; $T < 150^\circ\text{C}$), the Mai'iu fault is a true low-angle
931 normal fault, dipping $\sim 22 \pm 2^\circ$, and is highly misoriented. This situation is probably
932 overcome by the fault having a relatively low effective coefficient of friction there
933 ($\mu < 0.38$, saponite-rich gouge).

934 Acknowledgments, Samples, and Data

935 Marsden Fund grant VUW1310 provided financial support to conduct this research. We
936 are grateful to Hugh Davies (University of Papua New Guinea) and Ian Smith (University of
937 Auckland) for providing field book scans and discussions. We thank Susan Ellis, Samuel
938 Webber, Jürgen Österle, Laura Wallace, Kevin Norton, and Daniel Stockli for field support and
939 discussions. Special thanks go to the many landowners, oral chiefs, elders, and citizens who
940 granted us permission to study their land. We also thank our guides and carriers without whom
941 this work would not have been possible.

942 All structural data from the Suckling-Dayman Metamorphic Core Complex, raw EBSD
943 data of analysed calcite veins and MATLAB codes used in this study can be obtained from the
944 Data Repository (Mizera et al., 2021: <http://dx.doi.org/10.17632/mkpgbs4hf3.1>). Additional
945 information on fault rocks analyzed in this study can be found in the research archive of Victoria
946 University of Wellington (<http://hdl.handle.net/10063/8666>, Mizera, 2019).

947 References

- 948 Abers, G. A. (2009). Slip on shallow-dipping normal faults. *Geology*, 37(8), 767-768.
949 <https://doi.org/10.1130/focus082009.1>.
- 950 Abers, G. A., Eilon, Z., Gaherty, J. B., Jin, G., Kim, Y. H., Obrebski, M., & Dieck, C. (2016).
951 Southeast Papuan crustal tectonics: Imaging extension and buoyancy of an active rift.
952 *Journal of Geophysical Research: Solid Earth*, 121(2), 951-971.
953 <https://doi.org/10.1002/2015jb012621>
- 954 Anderson, E. M. (1951). *The dynamics of faulting and dyke formation: with applications to*
955 *Britain*. Edinburgh and London: Oliver and Boyd.
- 956 Angelier, J. T., & Mechler, P. (1977). Sur une methode graphique de recherche des contraintes
957 principales egalement utilisables en tectonique et en seismologie: la methode des diedres
958 droits. *Bulletin de la Société géologique de France*, 7(6), 1309-1318.
- 959 Axen, G. J. (1992). Pore pressure, stress increase, and fault weakening in low-angle normal
960 faulting. *Journal of Geophysical Research: Solid Earth*, 97(B6), 8979-8991.
961 <https://doi.org/10.1029/92JB00517>

- 962 Axen, G. J., & Selverstone, J. (1994). Stress state and fluid-pressure level along the Whipple
963 detachment fault, California. *Geology*, 22(9), 835-838. [https://doi.org/10.1130/0091-7613\(1994\)022%3C0835:SSAFPL%3E2.3.CO;2](https://doi.org/10.1130/0091-7613(1994)022%3C0835:SSAFPL%3E2.3.CO;2)
- 965 Axen, G. J., & Hartley, J. M. (1997). Field tests of rolling hinges: Existence, mechanical types,
966 and implications for extensional tectonics. *Journal of Geophysical Research: Solid Earth*,
967 102(B9), 20515–20537. <https://doi.org/10.1029/97JB01355>
- 968 Axen, G. J. (2004). Low-angle normal fault mechanics and crustal strength. In G. Karner (Ed.),
969 *Rheology and deformation of the lithosphere* (pp. 46–91). New York, NY: Columbia
970 University Press.
- 971 Axen, G. J. (2007). Research Focus: Significance of large-displacement, low-angle normal
972 faults. *Geology*, 35(3), 287–288. [https://doi.org/10.1130/0091-7613\(2007\)35\[287:rfsoll\]2.0.co;2](https://doi.org/10.1130/0091-7613(2007)35[287:rfsoll]2.0.co;2)
- 974 Barber, D. J., & Wenk, H. R. (1979). Deformation twinning in calcite, dolomite, and other
975 rhombohedral carbonates. *Physics and Chemistry of Minerals*, 5(2), 141-165.
976 <https://doi.org/10.1007/BF00307550>
- 977 Behr, W. M., & Platt, J. P. (2011). A naturally constrained stress profile through the middle crust
978 in an extensional terrane. *Earth and Planetary Science Letters*, 303(3-4), 181-192.
979 <https://doi.org/10.1016/j.epsl.2010.11.044>
- 980 Behr, W. M., & Platt, J. P. (2014). Brittle faults are weak, yet the ductile middle crust is strong:
981 Implications for lithospheric mechanics. *Geophysical Research Letters*, 41(22), 8067-
982 8075. <https://doi.org/10.1002/2014GL061349>
- 983 Bevins, R. E., Robinson, D., & Rowbotham, G. (1991). Compositional variations in mafic
984 phyllosilicates from regional low-grade metabasites and application of the chlorite
985 geothermometer. *Journal of Metamorphic Geology*, 9(6), 711–721.
986 <https://doi.org/10.1111/j.1525-1314.1991.tb00560.x>
- 987 Biemiller, J., Ellis, S., Mizera, M., Little, T., Wallace, L., & Lavier, L. (2019). Tectonic
988 inheritance following failed continental subduction: A model for core complex formation
989 in cold, strong lithosphere. *Tectonics*, 38(5), 1742–1763.
990 <https://doi.org/10.1029/2018TC005383>
- 991 Biemiller, J., Boulton, C., Wallace, L., Ellis, S., Little, T., Mizera, M., et al. (2020). Mechanical
992 implications of creep and partial coupling on the world's fastest slipping low-angle

- 993 normal fault in southeastern Papua New Guinea. *Journal of Geophysical Research: Solid*
 994 *Earth*, 125(10). <https://doi.org/10.1029/2020jb020117>
- 995 Bonifacie, M., Calmels, D., Eiler, J. M., Horita, J., Chaduteau, C., Vasconcelos, C., ... &
 996 Bourrand, J. J. (2017). Calibration of the dolomite clumped isotope thermometer from 25
 997 to 350 C, and implications for a universal calibration for all (Ca, Mg, Fe) CO₃
 998 carbonates. *Geochimica et Cosmochimica Acta*, 200, 255-279.
 999 <https://doi.org/10.1016/j.gca.2016.11.028>
- 1000 Bourdelle, F., & Cathelineau, M. (2015). Low-temperature chlorite geothermometry: A graphical
 1001 representation based on a T-R₂+Si diagram. *European Journal of Mineralogy*, 27(5),
 1002 617–626. <https://doi.org/10.1127/ejm/2015/0027-2467>
- 1003 Brand, W. A., Assonov, S. S., & Coplen, T. B. (2010). Correction for the ¹⁷O interference in δ
 1004 (¹³C) measurements when analyzing CO₂ with stable isotope mass spectrometry
 1005 (IUPAC Technical Report). *Pure and Applied Chemistry*, 82(8), 1719-1733.
 1006 <https://doi.org/10.1351/PAC-REP-09-01-05>
- 1007 Brandstätter, J., Kurz, W., & Rogowitz, A. (2017). Microstructural analysis and calcite
 1008 piezometry on hydrothermal veins: Insights into the deformation history of the Cocos
 1009 Plate at Site U1414 (IODP Expedition 344). *Tectonics*, 36(8), 1562-1579.
 1010 <https://doi.org/10.1002/2017TC004490>
- 1011 Buck, W. R. (1990). Comment on “Origin of regional, rooted low-angle normal faults: A
 1012 mechanical model and its tectonic implications” by An Yin. *Tectonics*, 9(3), 545–546.
 1013 <https://doi.org/10.1029/TC009i003p00545>
- 1014 Burkhard, M. (1993). Calcite twins, their geometry, appearance and significance as stress-strain
 1015 markers and indicators of tectonic regime: a review. *Journal of structural geology*, 15(3-
 1016 5), 351-368. [https://doi.org/10.1016/0191-8141\(93\)90132-T](https://doi.org/10.1016/0191-8141(93)90132-T)
- 1017 Byerlee, J. (1978). Friction of rocks. *Pure and applied geophysics*, 116(4-5), 615-626.
- 1018 Cathelineau, M. (1988). Cation site occupancy in chlorites and illites as function of temperature.
 1019 *Clay Minerals*, 23(4), 471–485. <https://doi.org/10.1180/claymin.1988.023.4.13>
- 1020 Chester, J. S., & Fletcher, R. C. (1997). Stress distribution and failure in anisotropic rock near a
 1021 bend on a weak fault. *Journal of Geophysical Research: Solid Earth*, 102(B1), 693-708.
 1022 <https://doi.org/10.1029/96JB02791>

- 1023 Chester, F. M., & Chester, J. S. (2000). Stress and deformation along wavy frictional faults.
1024 *Journal of Geophysical Research: Solid Earth*, 105(B10), 23421-23430.
1025 <https://doi.org/10.1029/2000JB900241>
- 1026 Chiaraluce, L., Chiarabba, C., Collettini, C., Piccinini, D., & Cocco, M. (2007). Architecture and
1027 mechanics of an active low-angle normal fault: Alto Tiberina fault, Northern Apennines,
1028 Italy. *Journal of Geophysical Research*, 112(B10). <https://doi.org/10.1029/2007JB005015>
- 1029 Chiaraluce, L., Amato, A., Carannante, S., Castelli, V., Cattaneo, M., Cocco, M., & Marzorati, S.
1030 (2014). The Alto Tiberina near fault observatory (Northern Apennines, Italy). *Annals of*
1031 *Geophysics*, 57(3), 1–16. <https://doi.org/10.4401/ag-6426>
- 1032 Choi, E., & Buck, W. R. (2012). Constraints on the strength of faults from the geometry of rider
1033 blocks in continental and oceanic core complexes. *Journal of Geophysical Research*,
1034 117(B4). <https://doi.org/10.1029/2011JB008741>
- 1035 Collettini, C., & Sibson, R. H. (2001). Normal faults, normal friction? *Geology*, 29(10), 927–
1036 930. [https://doi.org/10.1130/0091-7613\(2001\)029<0927:NFNF>2.0.CO;2](https://doi.org/10.1130/0091-7613(2001)029<0927:NFNF>2.0.CO;2)
- 1037 Collettini, C., & Barchi, M. R. (2004). A comparison of structural data and seismic images for
1038 low-angle normal faults in the Northern Apennines (Central Italy): constraints on activity.
1039 *Geological Society, London, Special Publications*, 224(1), 95-112.
1040 <https://doi.org/10.1144/GSL.SP.2004.224.01.07>
- 1041 Collettini, C., Niemeijer, A., Viti, C., & Marone, C. (2009a). Fault zone fabric and fault
1042 weakness. *Nature*, 462(7275), 907–910. <https://doi.org/10.1038/nature08585>
- 1043 Collettini, C., Viti, C., Smith, S. A., & Holdsworth, R. E. (2009b). Development of
1044 interconnected talc networks and weakening of continental low-angle normal faults.
1045 *Geology*, 37(6), 567-570. <https://doi.org/10.1130/G25645A.1>
- 1046 Collettini, C. (2011). The mechanical paradox of low-angle normal faults: Current understanding
1047 and open questions. *Tectonophysics*, 510(3), 253–268.
1048 <https://doi.org/10.1016/j.tecto.2011.07.015>
- 1049 Cooper, F. J., Platt, J. P., & Behr, W. M. (2017). Rheological transitions in the middle crust:
1050 Insights from Cordilleran metamorphic core complexes. *Solid Earth*, 8(1), 199.
1051 <https://doi.org/10.5194/se-8-199-2017>

- 1052 Craddock, J. P., & Magloughlin, J. F. (2005). Calcite strains, kinematic indicators, and magnetic
 1053 flow fabric of a Proterozoic pseudotachylite swarm, Minnesota River valley, USA.
 1054 *Tectonophysics*, 402(1-4), 153-168. <https://doi.org/10.1016/j.tecto.2004.12.035>
- 1055 Cross, A. J., Prior, D. J., Stipp, M., & Kidder, S. (2017). The recrystallized grain size piezometer
 1056 for quartz: An EBSD-based calibration. *Geophysical Research Letters*, 44(13), 6667-
 1057 6674. <https://doi.org/10.1002/2017GL073836>
- 1058 Daczko, N. R., Caffi, P., Halpin, J. A., & Mann, P. (2009). Exhumation of the Dayman dome
 1059 metamorphic core complex, eastern Papua New Guinea. *Journal of Metamorphic
 1060 Geology*, 27(6), 405–422. <https://doi.org/10.1111/j.1525-1314.2009.00825.x>
- 1061 Daczko, N. R., Caffi, P., & Mann, P. (2011). Structural evolution of the Dayman dome
 1062 metamorphic core complex, eastern Papua New Guinea. *Bulletin*, 123(11–12), 2335–
 1063 2351. <https://doi.org/10.1130/B30326.1>
- 1064 Davies, H. L. (1978). Folded thrust fault and associated metamorphism in the Suckling-Dayman
 1065 massif, Papua New Guinea. *Geological Survey of Papua New Guinea*, 280-A, 171–191.
- 1066 De Bresser, J. H. P., & Spiers, C. J. (1997). Strength characteristics of the r, f, and c slip systems
 1067 in calcite. *Tectonophysics*, 272(1), 1-23. [https://doi.org/10.1016/S0040-1951\(96\)00273-9](https://doi.org/10.1016/S0040-1951(96)00273-9)
- 1068 Dennis, K. J., & Schrag, D. P. (2010). Clumped isotope thermometry of carbonatites as an
 1069 indicator of diagenetic alteration. *Geochimica et Cosmochimica Acta*, 74(14), 4110-4122.
 1070 <https://doi.org/10.1016/j.gca.2010.04.005>
- 1071 Di Toro, G., Nielsen, S., & Pennacchioni, G. (2005). Earthquake rupture dynamics frozen in
 1072 exhumed ancient faults. *Nature*, 436(7053), 1009. <https://doi.org/10.1038/nature03910>
- 1073 Eiler, J. M. (2011). Paleoclimate reconstruction using carbonate clumped isotope thermometry.
 1074 *Quaternary Science Reviews*, 30(25-26), 3575-3588.
 1075 <https://doi.org/10.1016/j.quascirev.2011.09.001>
- 1076 Engelder, T. (1979). Mechanisms for strain within the Upper Devonian clastic sequence of the
 1077 Appalachian Plateau, western New York. *American Journal of Science*, 279(5), 527-542.
 1078 <https://doi.org/10.2475/ajs.279.5.527>
- 1079 Evans, M. A., & Dunne, W. M. (1991). Strain factorization and partitioning in the North
 1080 Mountain thrust sheet, central Appalachians, USA. *Journal of Structural Geology*, 13(1),
 1081 21-35. [https://doi.org/10.1016/0191-8141\(91\)90098-4](https://doi.org/10.1016/0191-8141(91)90098-4)

- 1082 Faulkner, D. R., Mitchell, T. M., Healy, D., & Heap, M. J. (2006). Slip on 'weak' faults by the
 1083 rotation of regional stress in the fracture damage zone. *Nature*, 444(7121), 922.
 1084 <https://doi.org/10.1038/nature05353>
- 1085 Ferrill, D. A. (1998). Critical re-evaluation of differential stress estimates from calcite twins in
 1086 coarse-grained limestone. *Tectonophysics*, 285(1-2), 77-86.
 1087 [https://doi.org/10.1016/S0040-1951\(97\)00190-X](https://doi.org/10.1016/S0040-1951(97)00190-X)
 1088
- 1089 Ferrill, D. A., Morris, A. P., Evans, M. A., Burkhard, M., Groshong Jr, R. H., & Onasch, C. M.
 1090 (2004). Calcite twin morphology: a low-temperature deformation geothermometer.
 1091 *Journal of structural Geology*, 26(8), 1521-1529.
 1092 <https://doi.org/10.1016/j.jsg.2003.11.028>
- 1093 Fitz, G., & Mann, P. (2013). Tectonic uplift mechanism of the Goodenough and Fergusson
 1094 Island gneiss domes, eastern Papua New Guinea: Constraints from seismic reflection and
 1095 well data. *Geochemistry, Geophysics, Geosystems*, 14(10), 3969-3995.
 1096 <https://doi.org/10.1002/ggge.20208>
- 1097 Fletcher, J. M., Bartley, J. M., Martin, M. W., Glazner, A. F., & Walker, J. D. (1995). Large-
 1098 magnitude continental extension: An example from the central Mojave metamorphic core
 1099 complex. *Geological Society of America Bulletin*, 107(12), 1468-1483.
 1100 [https://doi.org/10.1130/0016-7606\(1995\)107%3C1468:LMCEAE%3E2.3.CO;2](https://doi.org/10.1130/0016-7606(1995)107%3C1468:LMCEAE%3E2.3.CO;2)
- 1101 Floyd, J. S., Mutter, J. C., Goodliffe, A. M., & Taylor, B. (2001). Evidence for fault weakness
 1102 and fluid flow within an active low-angle normal fault. *Nature*, 411(6839), 779.
 1103 <https://doi.org/10.1038/35081040>
- 1104 Fynn, G. W., & Powell, W. J. A. (1979). *The cutting and polishing of electro-optic materials*.
 1105 Bristol, Hilger. - 215 p.
- 1106 Ghosh, P., Adkins, J., Affek, H., Balta, B., Guo, W., Schauble, E. A., ... & Eiler, J. M. (2006).
 1107 13C–18O bonds in carbonate minerals: a new kind of paleothermometer. *Geochimica et*
 1108 *Cosmochimica Acta*, 70(6), 1439-1456. <https://doi.org/10.1016/j.gca.2005.11.014>
- 1109 Groshong Jr, R. H. (1972). Strain calculated from twinning in calcite. *Geological Society of*
 1110 *America Bulletin*, 83(7), 2025-2038. [https://doi.org/10.1130/0016-](https://doi.org/10.1130/0016-7606(1972)83[2025:SCFTIC]2.0.CO;2)
 1111 [7606\(1972\)83\[2025:SCFTIC\]2.0.CO;2](https://doi.org/10.1130/0016-7606(1972)83[2025:SCFTIC]2.0.CO;2)

- 1112 Groshong Jr, R. H. (1974). Experimental test of least-squares strain gage calculation using
1113 twinned calcite. *Geological Society of America Bulletin*, 85(12), 1855-1864.
1114 [https://doi.org/10.1130/0016-7606\(1974\)85%3C1855:ETOLSG%3E2.0.CO;2](https://doi.org/10.1130/0016-7606(1974)85%3C1855:ETOLSG%3E2.0.CO;2)
- 1115 Groshong Jr, R. H. (1975). Strain, fractures, and pressure solution in natural single-layer folds.
1116 *Geological Society of America Bulletin*, 86(10), 1363-1376.
1117 [https://doi.org/10.1130/0016-7606\(1975\)86%3C1363:SFAPSI%3E2.0.CO;2](https://doi.org/10.1130/0016-7606(1975)86%3C1363:SFAPSI%3E2.0.CO;2)
- 1118 Groshong Jr, R. H., Teufel, L. W., & Gasteiger, C. (1984). Precision and accuracy of the calcite
1119 strain-gage technique. *Geological Society of America Bulletin*, 95(3), 357-363.
1120 [https://doi.org/10.1130/0016-7606\(1984\)95%3C357:PAAOTC%3E2.0.CO;2](https://doi.org/10.1130/0016-7606(1984)95%3C357:PAAOTC%3E2.0.CO;2)
- 1121 Groshong Jr, R. H. (1988). Low-temperature deformation mechanisms and their interpretation.
1122 *Geological Society of America Bulletin*, 100(9), 1329-1360.
1123 [https://doi.org/10.1130/0016-7606\(1988\)100%3C1329:LTDMAT%3E2.3.CO;2](https://doi.org/10.1130/0016-7606(1988)100%3C1329:LTDMAT%3E2.3.CO;2)
- 1124 Hayman, N. W., Knott, J. R., Cowan, D. S., Nemser, E., & Sarna-Wojcicki, A. M. (2003).
1125 Quaternary low-angle slip on detachment faults in Death Valley, California. *Geology*,
1126 31(4), 343-346. [https://doi.org/10.1130/0091-](https://doi.org/10.1130/0091-7613(2003)031%3C0343:QLASOD%3E2.0.CO;2)
1127 [7613\(2003\)031%3C0343:QLASOD%3E2.0.CO;2](https://doi.org/10.1130/0091-7613(2003)031%3C0343:QLASOD%3E2.0.CO;2)
- 1128 Hickman, S., & Zoback, M. (2004). Stress orientations and magnitudes in the SAFOD pilot hole.
1129 *Geophysical Research Letters*, 31(15). <https://doi.org/10.1029/2004GL020043>
- 1130 Hreinsdóttir, S., & Bennett, R. A. (2009). Active aseismic creep on the Alto Tiberina low-angle
1131 normal fault. *Geology*, 37(8), 683–686. <https://doi.org/10.1130/G30194A.1>
- 1132 Huntington, K. W., Eiler, J. M., Affek, H. P., Guo, W., Bonifacie, M., Yeung, L. Y., ... & Came,
1133 R. (2009). Methods and limitations of ‘clumped’CO₂ isotope ($\Delta 47$) analysis by gas-
1134 source isotope ratio mass spectrometry. *Journal of Mass Spectrometry*, 44(9), 1318-1329.
1135 <https://doi.org/10.1002/jms.1614>
- 1136 Ikari, M. J., Saffer, D. M., & Marone, C. (2009). Frictional and hydrologic properties of clay-rich
1137 fault gouge. *Journal of Geophysical Research: Solid Earth*, 114(B5).
1138 <https://doi.org/10.1029/2008JB006089>
- 1139 Jamison, W. R., & Spang, J. H. (1976). Use of calcite twin lamellae to infer differential stress.
1140 *Geological Society of America Bulletin*, 87(6), 868-872. [https://doi.org/10.1130/0016-](https://doi.org/10.1130/0016-7606(1976)87%3C868:UOCTLT%3E2.0.CO;2)
1141 [7606\(1976\)87%3C868:UOCTLT%3E2.0.CO;2](https://doi.org/10.1130/0016-7606(1976)87%3C868:UOCTLT%3E2.0.CO;2)

- 1142 Jaya, A., & Nishikawa, O. (2013). Paleostress reconstruction from calcite twin and fault–slip
1143 data using the multiple inverse method in the East Walanae fault zone: Implications for
1144 the Neogene contraction in South Sulawesi, Indonesia. *Journal of Structural Geology*, 55,
1145 34-49. <https://doi.org/10.1016/j.jsg.2013.07.006>
- 1146 Kanai, T., & Takagi, H. (2016). Determination of the stress conditions of the ductile-to-brittle
1147 regime along the Asuke Shear Zone, SW Japan. *Journal of Structural Geology*, 85, 154-
1148 167. <https://doi.org/10.1016/j.jsg.2016.02.009>
- 1149 Kilsdonk, B., & Wiltschko, D. V. (1988). Deformation mechanisms in the southeastern ramp
1150 region of the Pine Mountain block, Tennessee. *Geological Society of America Bulletin*,
1151 100(5), 653-664. [https://doi.org/10.1130/0016-
1152 7606\(1988\)100%3C0653:DMITSR%3E2.3.CO;2](https://doi.org/10.1130/0016-7606(1988)100%3C0653:DMITSR%3E2.3.CO;2)
- 1153 Lacombe, O., & Laurent, P. (1996). Determination of deviatoric stress tensors based on inversion
1154 of calcite twin data from experimentally deformed monophase samples: preliminary
1155 results. *Tectonophysics*, 255(3-4), 189-202. [https://doi.org/10.1016/0040-1951\(95\)00136-
1156 0](https://doi.org/10.1016/0040-1951(95)00136-0)
- 1157 Lindley, I. D. (2014). Suckling dome and the Australian–Woodlark plate boundary in eastern
1158 Papua: The geology of the Keveri and Ada'u Valleys. *Australian Journal of Earth
1159 Sciences*, 61(8), 1125–1147. <https://doi.org/10.1080/08120099.2014.965980>
- 1160 Lister, G. S., & Davis, G. A. (1989). The origin of metamorphic core complexes and detachment
1161 faults formed during Tertiary continental extension in the northern Colorado River
1162 region, USA. *Journal of Structural Geology*, 11(1), 65–94. [https://doi.org/10.1016/0191-
1163 8141\(89\)90036-9](https://doi.org/10.1016/0191-8141(89)90036-9)
- 1164 Little, T. A., Baldwin, S. L., Fitzgerald, P. G., & Monteleone, B. (2007). Continental rifting and
1165 metamorphic core complex formation ahead of the woodlark spreading ridge,
1166 D'Entrecasteaux Islands, Papua New Guinea. *Tectonics*, 26(1).
1167 <https://doi.org/10.1029/2005TC001911>
- 1168 Little, T. A., Hacker, B. R., Gordon, S. M., Baldwin, S. L., Fitzgerald, P. G., Ellis, S., &
1169 Korchinski, M. (2011). Diapiric exhumation of Earth's youngest (UHP) eclogites in the
1170 gneiss domes of the D'Entrecasteaux Islands, Papua New Guinea. *Tectonophysics*,
1171 510(1), 39-68. <https://doi.org/10.1016/j.tecto.2011.06.006>

- 1172 Little, T. A., Webber, S. M., Mizera, M., Boulton, C., Oesterle, J., Ellis, S., Boles, A., van der
 1173 Pluijm, B., Norton, K., Seward, D., Biemiller, J., and Wallace, L. (2019): Evolution of a
 1174 rapidly slipping, active low-angle normal fault, Suckling-Dayman Metamorphic Core
 1175 Complex, SE Papua New Guinea. <https://doi.org/10.1130/b35051.1>
- 1176 Lockner, D. A., Morrow, C., Moore, D., & Hickman, S. (2011). Low strength of deep San
 1177 Andreas fault gouge from SAFOD core. *Nature*, 472(7341), 82.
 1178 <https://doi.org/10.1038/nature09927>
- 1179 Martinez, F., Goodliffe, A. M., & Taylor, B. (2001). Metamorphic core complex formation by
 1180 density inversion and lower-crust extrusion. *Nature*, 411(6840), 930.
 1181 <https://doi.org/10.1038/35082042>
- 1182 Mello, M., Bhat, H. S., Rosakis, A. J., & Kanamori, H. (2010). Identifying the unique ground
 1183 motion signatures of supershear earthquakes: Theory and experiments. *Tectonophysics*,
 1184 493(3-4), 297-326. <https://doi.org/10.1016/j.tecto.2010.07.003>
- 1185 Mizera, M. (2019). Deformational processes accommodating slip on an active low-angle normal
 1186 fault, Suckling-Dayman Metamorphic Core Complex, Papua New Guinea, (Doctoral
 1187 dissertation). Wellington, New Zealand: Victoria University of Wellington. Retrieved
 1188 from <http://hdl.handle.net/10063/8666>
- 1189 Mizera, M., Little, T. A., Biemiller, J., Ellis, S., Webber, S., & Norton, K. P. (2019). Structural
 1190 and geomorphic evidence for rolling-hinge style deformation of an active continental
 1191 low-angle normal fault, SE Papua New Guinea. *Tectonics*, 38(5), 1556–1583.
 1192 <https://doi.org/10.1029/2018TC005167>
- 1193 Mizera, M., Little, T., Prior, D. J. & Smith, E. G. C. (2021). Strength and Stress Evolution of the
 1194 Active Mai'iu Low-Angle Normal Fault, Data Repository. Mendeley Data, V1.
 1195 <http://dx.doi.org/10.17632/mkpgbs4hf3.1>
- 1196 Mizera, M., Little, T., Boulton, C., Prior, D., Watson, E., Biemiller, J., ... & Shigematsu, N.
 1197 (2020). Slow-to-Fast Deformation in Mafic Fault Rocks on an Active Low-Angle Normal
 1198 Fault, Woodlark Rift, SE Papua New Guinea. *Geochemistry, Geophysics, Geosystems*,
 1199 e2020GC009171. <https://doi.org/10.1029/2020GC009171>
- 1200 Morrow, C. A., Moore, D. E., & Lockner, D. A. (2017). Frictional strength of wet and dry
 1201 montmorillonite. *Journal of Geophysical Research: Solid Earth*, 122(5), 3392-3409.
 1202 <https://doi.org/10.1002/2016JB013658>

- 1203 Österle, J. (2019). The thermo-tectonic evolution of the Suckling-Dayman metamorphic core
1204 complex, southeastern Papua New Guinea (Doctoral dissertation, Victoria University of
1205 Wellington). <https://hdl.handle.net/10063/8241>
- 1206 Österle, J. E., Little, T. A., Seward, D., Stockli, D. F., & Gamble, J. (2020). The petrology,
1207 geochronology and tectono-magmatic setting of igneous rocks in the Suckling-Dayman
1208 metamorphic core complex, Papua New Guinea. *Gondwana Research*, 83, 390–414.
1209 <https://doi.org/10.1016/j.gr.2020.01.014>
- 1210 Otsubo, M., & Yamaji, A. (2006). Improved resolution of the multiple inverse method by
1211 eliminating erroneous solutions. *Computers & geosciences*, 32(8), 1221-1227.
1212 <https://doi.org/10.1016/j.cageo.2005.10.022>
- 1213 Otsubo, M., Yamaji, A., & Kubo, A. (2008). Determination of stresses from heterogeneous focal
1214 mechanism data: An adaptation of the multiple inverse method. *Tectonophysics*, 457(3-
1215 4), 150-160. <https://doi.org/10.1016/j.tecto.2008.06.012>
- 1216 Passey, B. H., Levin, N. E., Cerling, T. E., Brown, F. H., & Eiler, J. M. (2010). High-
1217 temperature environments of human evolution in East Africa based on bond ordering in
1218 paleosol carbonates. *Proceedings of the National Academy of Sciences*, 107(25), 11245-
1219 11249. <https://doi.org/10.1073/pnas.1001824107>
- 1220 Passey, B. H., & Henkes, G. A. (2012). Carbonate clumped isotope bond reordering and
1221 geospeedometry. *Earth and Planetary Science Letters*, 351, 223-236.
1222 <https://doi.org/10.1016/j.epsl.2012.07.021>
- 1223 Platt, J. P., Behr, W. M., & Cooper, F. J. (2015). Metamorphic core complexes: Windows into
1224 the mechanics and rheology of the crust. *Journal of the Geological Society*, 172(1), 9–27.
1225 <https://doi.org/10.1144/jgs2014-036>
- 1226 Platt, J. P., & De Bresser, J. H. P. (2017). Stress dependence of microstructures in experimentally
1227 deformed calcite. *Journal of Structural Geology*, 105, 80-87.
1228 <https://doi.org/10.1016/j.jsg.2017.10.012>
- 1229 Reston, T. (2020). On the rotation and frictional lock-up of normal faults: Explaining the dip
1230 distribution of normal fault earthquakes and resolving the low-angle normal fault
1231 paradox. *Tectonophysics*, 790, 228550. <https://doi.org/10.1016/j.tecto.2020.228550>
- 1232 Rigo, A., Lyon-Caen, H., Armijo, R., Deschamps, A., Hatzfeld, D., Makropoulos, K., &
1233 Kassaras, I. (1996). A microseismic study in the western part of the Gulf of Corinth

- 1234 (Greece): Implications for large-scale normal faulting mechanisms. *Geophysical Journal*
1235 *International*, 126(3), 663–688. <https://doi.org/10.1111/j.1365-246X.1996.tb04697.x>
- 1236 Rowe, K. J., & Rutter, E. H. (1990). Palaeostress estimation using calcite twinning: experimental
1237 calibration and application to nature. *Journal of Structural Geology*, 12(1), 1-17.
1238 [https://doi.org/10.1016/0191-8141\(90\)90044-Y](https://doi.org/10.1016/0191-8141(90)90044-Y)
- 1239 Rutter, E. H., Faulkner, D. R., Brodie, K. H., Phillips, R. J., & Searle, M. P. (2007). Rock
1240 deformation processes in the Karakoram fault zone, Eastern Karakoram, Ladakh, NW
1241 India. *Journal of Structural Geology*, 29(8), 1315-1326.
1242 <https://doi.org/10.1016/j.jsg.2007.05.001>
- 1243 Ryb, U., Lloyd, M. K., Stolper, D. A., & Eiler, J. M. (2017). The clumped-isotope geochemistry
1244 of exhumed marbles from Naxos, Greece. *Earth and Planetary Science Letters*, 470, 1-12.
1245 <https://doi.org/10.1016/j.epsl.2017.04.026>
- 1246 Rybacki, E., Evans, B., Janssen, C., Wirth, R., & Dresen, G. (2013). Influence of stress,
1247 temperature, and strain on calcite twins constrained by deformation experiments.
1248 *Tectonophysics*, 601, 20-36. <https://doi.org/10.1016/j.tecto.2013.04.021>
- 1249 Schultz, R. A. (1993). Brittle strength of basaltic rock masses with applications to Venus. *Journal*
1250 *of Geophysical Research: Planets*, 98(E6), 10883-10895.
1251 <https://doi.org/10.1029/93JE00691>
- 1252 Sibson, R. H. (1985). A note on fault reactivation. *Journal of Structural Geology*, 7(6), 751–754.
1253 [https://doi.org/10.1016/0191-8141\(85\)90150-6](https://doi.org/10.1016/0191-8141(85)90150-6)
- 1254 Singleton, J. S. (2013). Development of extension-parallel corrugations in the Buckskin-Rawhide
1255 metamorphic core complex, west-central Arizona. *Bulletin*, 125(3-4), 453-472.
1256 <https://doi.org/10.1130/B30672.1>
- 1257 Smith, I. E., & Davies, H. L. (1976). *Geology of the southeast Papuan mainland*. Bureau of
1258 mineral resources, geology and geophysics. Canberra, ACT: Australian Publishing
1259 Service.
- 1260 Speckbacher, R., Behrmann, J. H., Nagel, T. J., Stipp, M., & Mahlke, J. (2012). Fluid flow and
1261 metasomatic fault weakening in the Moresby Seamount detachment, Woodlark Basin,
1262 offshore Papua New Guinea. *Geochemistry, Geophysics, Geosystems*, 13(11).
1263 <https://doi.org/10.1029/2012GC004407>

- 1264 Speckbacher, R., Stipp, M., Behrmann, J. H., & Heidelbach, F. (2013). Fluid-assisted fracturing,
1265 cataclasis, and resulting plastic flow in mylonites from the Moresby Seamount
1266 detachment, Woodlark Basin. *Journal of Structural Geology*, 56, 156–171.
1267 <https://doi.org/10.1016/j.jsg.2013.10.001>
- 1268 Spencer, J. E. (2010). Structural analysis of three extensional detachment faults with data from
1269 the 2000 Space-Shuttle Radar Topography Mission. *Geological Society of America*
1270 *Today*, 20(8), 4–10. <https://doi.org/10.1130/GSATG59A.1>
- 1271 Stolper, D. A., & Eiler, J. M. (2015). The kinetics of solid-state isotope-exchange reactions for
1272 clumped isotopes: A study of inorganic calcites and apatites from natural and
1273 experimental samples. *American Journal of Science*, 315(5), 363–411.
1274 <https://doi.org/10.2475/05.2015.01>
- 1275 Taylor, B., & Huchon, P. (2002). Active continental extension in the western Woodlark Basin: A
1276 synthesis of Leg 180 results. In P. Huchon, B. Taylor, & A. Klaus (Eds.), *Proc. ODP, Sci.*
1277 *Results* (Vol. 180, pp. 1–36). College Station, TX: Ocean Drilling Program.
1278 <https://doi.org/10.2973/odp.proc.sr.180.150.2002>
- 1279 Tjhin, K. T. (1976). Trobriand Basin exploration, Papua New Guinea. *The APPEA Journal*,
1280 16(1), 81–90. <https://doi.org/10.1071/AJ75008>
- 1281 Tregoning, P., Lambeck, K., Stolz, A., Morgan, P., McClusky, S. C., Beek, P., & Murphy, B.
1282 (1998). Estimation of current plate motions in Papua New Guinea from global
1283 positioning system observations. *Journal of Geophysical Research*, 103(B6), 12181–
1284 12203. <https://doi.org/10.1029/97JB03676>
- 1285 Tullis, T. E. (1980). The use of mechanical twinning in minerals as a measure of shear stress
1286 magnitudes. *Journal of Geophysical Research: Solid Earth*, 85(B11), 6263–6268.
1287 <https://doi.org/10.1029/JB085iB11p06263>
- 1288 Turner, F. J. (1953). Nature and dynamic interpretation of deformation lamellae in calcite of
1289 three marbles. *American Journal of Science*, 251(4), 276–298.
1290 <https://doi.org/10.2475/ajs.251.4.276>
- 1291 Turner, F. J. (1962, January). Compression and tension axes deduced from (0112) Twinning in
1292 Calcite. In *Journal of Geophysical Research* (Vol. 67, No. 4, p. 1660). 2000 FLORIDA
1293 AVE NW, WASHINGTON, DC 20009: AMER GEOPHYSICAL UNION.

- 1294 Valcke, S. L. A., De Bresser, J. H. P., Pennock, G. M., & Drury, M. R. (2015). Influence of
 1295 deformation conditions on the development of heterogeneous recrystallization
 1296 microstructures in experimentally deformed Carrara marble. Geological Society, London,
 1297 Special Publications, 409(1), 175-200. <https://doi.org/10.1144/SP409.4>
- 1298 Wallace, L. M., Stevens, C., Silver, E., McCaffrey, R., Loratung, W., Hasiata, S., & Taugaloidi,
 1299 J. (2004). GPS and seismological constraints on active tectonics and arc-continent
 1300 collision in Papua New Guinea: Implications for mechanics of microplate rotations in a
 1301 plate boundary zone. *Journal of Geophysical Research*, 109(B5).
 1302 <https://doi.org/10.1029/2003JB002481>
- 1303 Wallace, L. M., Ellis, S., Little, T., Tregoning, P., Palmer, N., Rosa, R., & Kwazi, J. (2014).
 1304 Continental breakup and UHP rock exhumation in action: GPS results from the Woodlark
 1305 Rift, Papua New Guinea. *Geochemistry, Geophysics. Geosystems*, 15(11), 4267–4290.
 1306 <https://doi.org/10.1002/2014GC005458>
- 1307 Watson, E. J., Turner, G. M., Little, T. A., & Piispa, E. J. (2021). Using paleomagnetism to test
 1308 rolling hinge behaviour of an active continental low angle normal fault, Papua New
 1309 Guinea. *Earth and Planetary Science Letters*, 558, 116745.
- 1310 Webb, L. E., Baldwin, S. L., Little, T. A., & Fitzgerald, P. G. (2008). Can microplate rotation
 1311 drive subduction inversion?. *Geology*, 36(10), 823–826.
 1312 <https://doi.org/10.1130/G25134A.1>
- 1313 Webber, S., Norton, K. P., Little, T. A., Wallace, L. M., & Ellis, S. (2018). How fast can low-
 1314 angle normal faults slip? Insights from cosmogenic exposure dating of the active Mai'iu
 1315 fault, Papua New Guinea. *Geology*, 46(3), 227–230. <https://doi.org/10.1130/G39736.1>
- 1316 Webber, S., Little, T. A., Norton, K. P., Österle, J., Mizera, M., Seward, D., & Holden, G.
 1317 (2020). Progressive back-warping of a rider block atop an actively exhuming, continental
 1318 low-angle normal fault. *Journal of Structural Geology*, 130, 103906.
 1319 <https://doi.org/10.1016/j.jsg.2019.103906>
- 1320 Weber, J. C., Ferrill, D. A., & Roden-Tice, M. K. (2001). Calcite and quartz microstructural
 1321 geothermometry of low-grade metasedimentary rocks, Northern Range, Trinidad. *Journal*
 1322 *of Structural Geology*, 23(1), 93-112. [https://doi.org/10.1016/S0191-8141\(00\)00066-3](https://doi.org/10.1016/S0191-8141(00)00066-3)

- 1323 Westaway, R. (2005). Active low-angle normal faulting in the Woodlark extensional province,
 1324 Papua New Guinea: A physical model. *Tectonics*, 24(6).
 1325 <https://doi.org/10.1029/2004TC001744>
- 1326 Whitney, D. L., Teyssier, C., Rey, P., & Buck, W. R. (2013). Continental and oceanic core
 1327 complexes. *The Geological Society of America Bulletin*, 125(3–4), 273–298.
 1328 <https://doi.org/10.1130/B30754.1>
- 1329 Yamaji, A. (2000). The multiple inverse method: a new technique to separate stresses from
 1330 heterogeneous fault-slip data. *Journal of Structural Geology*, 22(4), 441–452.
 1331 [https://doi.org/10.1016/S0191-8141\(99\)00163-7](https://doi.org/10.1016/S0191-8141(99)00163-7)
- 1332 Yamaji, A., & Sato, K. (2006). Distances for the solutions of stress tensor inversion in relation to
 1333 misfit angles that accompany the solutions. *Geophysical Journal International*, 167(2),
 1334 933–942. <https://doi.org/10.1111/j.1365-246X.2006.03188.x>
- 1335 Yamaji, A. (2015). How tightly does calcite e-twin constrain stress?. *Journal of Structural*
 1336 *Geology*, 72, 83–95. <https://doi.org/10.1016/j.jsg.2015.01.008>
- 1337 Yin, A. (1989). Origin of regional, rooted low-angle normal faults: A mechanical model and its
 1338 tectonic implications. *Tectonics*, 8(3), 469–482.
 1339 <https://doi.org/10.1029/TC008i003p00469>
- 1340 Zoback, M. D., & Harjes, H. P. (1997). Injection-induced earthquakes and crustal stress at 9 km
 1341 depth at the KTB deep drilling site, Germany. *Journal of Geophysical Research: Solid*
 1342 *Earth*, 102(B8), 18477–18491. <https://doi.org/10.1029/96JB02814>

1343 **References from the Supporting Information**

- 1344 Angelier, J. (1979). Determination of the mean principal directions of stresses for a given fault
 1345 population. *Tectonophysics*, 56(3–4), T17–T26. [https://doi.org/10.1016/0040-](https://doi.org/10.1016/0040-1951(79)90081-7)
 1346 [1951\(79\)90081-7](https://doi.org/10.1016/0040-1951(79)90081-7)
- 1347 Barnhoorn, A., Bystricky, M., Burlini, L., & Kunze, K. (2004). The role of recrystallisation on
 1348 the deformation behaviour of calcite rocks: large strain torsion experiments on Carrara
 1349 marble. *Journal of Structural Geology*, 26(5), 885–903.
 1350 <https://doi.org/10.1016/j.jsg.2003.11.024>

- 1351 Caffi , P. (2008). Evolution of an Active Metamorphic Core Complex, Suckling-Dayman Massif,
1352 Eastern Papua New Guinea [B.Sc. (Honor's) thesis]: Sydney, Australia: Macquarie
1353 University, 113 p.
- 1354 De Bresser, J. H. P., Evans, B., & Renner, J. (2002). On estimating the strength of calcite rocks
1355 under natural conditions. *Geological Society, London, Special Publications*, 200(1), 309-
1356 329. <https://doi.org/10.1144/GSL.SP.2001.200.01.18>
- 1357 De Bresser, J. H. P., Urai, J. L., & Olgaard, D. L. (2005). Effect of water on the strength and
1358 microstructure of Carrara marble axially compressed at high temperature. *Journal of*
1359 *Structural Geology*, 27(2), 265-281. <https://doi.org/10.1016/j.jsg.2004.10.002>
- 1360 Ebert, A., Herwegh, M., Ramseyer, K., & Decrouez, D. (2008). Calcite microstructures as paleo-
1361 thermometer and indicator of shear zone width. *Geotectonic research*, 95(38), 36-38.
1362 <https://doi.org/10.1127/1864-5658/08/9501-0036>
- 1363 Etchecopar, A., Vasseur, G., & Daignieres, M. (1981). An inverse problem in microtectonics for
1364 the determination of stress tensors from fault striation analysis. *Journal of Structural*
1365 *Geology*, 3(1), 51-65. [https://doi.org/10.1016/0191-8141\(81\)90056-0](https://doi.org/10.1016/0191-8141(81)90056-0)
- 1366 Ferrill, D. A. (1991). Calcite twin widths and intensities as metamorphic indicators in natural
1367 low-temperature deformation of limestone. *Journal of Structural Geology*, 13(6), 667-
1368 675. [https://doi.org/10.1016/0191-8141\(91\)90029-I](https://doi.org/10.1016/0191-8141(91)90029-I)
- 1369 Karaman, K., Cihangir, F., & Kesimal, A. (2013). Kaya Malzemesinin Kohezyon ve İçsel
1370 Sürtünme Açısının Dolaylı Yöntemlerle İrdelenmesi. *Mehmet Akif Ersoy Üniversitesi*
1371 *Fen Bilimleri Enstitüsü Dergisi*, 4(2), 13-19. Retrieved from
1372 <https://dergipark.org.tr/en/pub/makufebed/issue/19420/206536>
- 1373 Ketcham, R. A. (1996). Thermal models of core-complex evolution in Arizona and New Guinea:
1374 Implications for ancient cooling paths and present-day heat flow. *Tectonics*, 15(5), 933-
1375 951. <https://doi.org/10.1029/96TC00033>
- 1376 Labuz J.F., Zang A. (2012). Mohr–Coulomb Failure Criterion. In: Ulusay R. (eds) *The ISRM*
1377 *Suggested Methods for Rock Characterization, Testing and Monitoring: 2007-2014*.
1378 Springer, Cham. https://doi.org/10.1007/978-3-319-07713-0_19
- 1379 O'Neil, J. R., & Taylor Jr, H. P. (1969). Oxygen isotope equilibrium between muscovite and
1380 water. *Journal of Geophysical Research*, 74(25), 6012-6022.
1381 <https://doi.org/10.1029/JB074i025p06012>

- 1382 Renner, J., Evans, B., & Siddiqi, G. (2002). Dislocation creep of calcite. *Journal of Geophysical*
 1383 *Research: Solid Earth*, 107(B12). <https://doi.org/10.1029/2001JB001680>
- 1384 Rutter, E. H. (1995). Experimental study of the influence of stress, temperature, and strain on the
 1385 dynamic recrystallization of Carrara marble. *Journal of Geophysical Research: Solid*
 1386 *Earth*, 100(B12), 24651-24663. <https://doi.org/10.1029/95JB02500>
- 1387 Rybacki, E., Janssen, C., Wirth, R., Chen, K., Wenk, H. R., Stromeyer, D., & Dresen, G. (2011).
 1388 Low-temperature deformation in calcite veins of SAFOD core samples (San Andreas
 1389 Fault)—microstructural analysis and implications for fault rheology. *Tectonophysics*,
 1390 509(1-2), 107-119. <https://doi.org/10.1016/j.tecto.2011.05.014>
- 1391 Schmid, S. M., Paterson, M. S., & Boland, J. N. (1980). High temperature flow and dynamic
 1392 recrystallization in Carrara marble. *Tectonophysics*, 65(3-4), 245-280.
 1393 [https://doi.org/10.1016/0040-1951\(80\)90077-3](https://doi.org/10.1016/0040-1951(80)90077-3)
- 1394 Sibson, R. H. (1998). Brittle failure mode plots for compressional and extensional tectonic
 1395 regimes. *Journal of Structural Geology*, 20(5), 655-660. [https://doi.org/10.1016/S0191-](https://doi.org/10.1016/S0191-8141(98)00116-3)
 1396 [8141\(98\)00116-3](https://doi.org/10.1016/S0191-8141(98)00116-3)
- 1397 Ter Heege, J. H., De Bresser, J. H. P., & Spiers, C. J. (2002). The influence of dynamic
 1398 recrystallization on the grain size distribution and rheological behaviour of Carrara
 1399 marble deformed in axial compression. *Geological Society, London, Special*
 1400 *Publications*, 200(1), 331-353. <https://doi.org/10.1144/GSL.SP.2001.200.01.19>
- 1401 Tielke, J. A. (2010). Development and application of a method for determining paleostress from
 1402 calcite deformation twins using electron backscatter diffraction: M.s. thesis, South
 1403 Dakota School of Mines and Technology, 133 p.
- 1404 Walker, A. N., Rutter, E. H., & Brodie, K. H. (1990). Experimental study of grain-size sensitive
 1405 flow of synthetic, hot-pressed calcite rocks. *Geological Society, London, Special*
 1406 *Publications*, 54(1), 259-284. <https://doi.org/10.1144/GSL.SP.1990.054.01.24>